

Research Articles | Systems/Circuits

Spike rate inference from mouse spinal cord calcium imaging data

<https://doi.org/10.1523/JNEUROSCI.1187-24.2025>

Received: 15 June 2024

Revised: 5 March 2025

Accepted: 14 March 2025

Copyright © 2025 Rupprecht et al.

This is an open-access article distributed under the terms of the [Creative Commons Attribution 4.0 International license](#), which permits unrestricted use, distribution and reproduction in any medium provided that the original work is properly attributed.

This Early Release article has been peer reviewed and accepted, but has not been through the composition and copyediting processes. The final version may differ slightly in style or formatting and will contain links to any extended data.

Alerts: Sign up at www.jneurosci.org/alerts to receive customized email alerts when the fully formatted version of this article is published.

1 **Title:**

2 Spike rate inference from mouse spinal cord calcium imaging data

3

4 **Abbreviated title:**

5 Spike inference from spinal cord calcium signals

6

7

8 **Author list:**

9 Peter Rupprecht^{1,2,*}, Wei Fan³, Steve J. Sullivan³, Fritjof Helmchen^{1,2,4}, Andrei D. Sdrulla^{3,*}

10

11 **Affiliations:**

12 ¹ Laboratory of Neural Circuit Dynamics, Brain Research Institute, University of Zurich, Zurich
13 CH-8057, Switzerland

14 ² Neuroscience Center Zurich, University of Zurich, Zurich CH-8057, Switzerland

15 ³ Department of Anesthesiology and Perioperative Medicine, Oregon Health & Science University,
16 Portland, Oregon 97239-3098, USA

17 ⁴ University Research Priority Program (URPP), Adaptive Brain Circuits in Development and
18 Learning, University of Zurich, Zurich CH-8057, Switzerland

19

20

21 **Corresponding authors:** rupprecht@hifo.uzh.ch, sdrulla@ohsu.edu

22

23 **Number of pages:** 25

24 **Number of figures:** 7, **tables:** 1, **multimedia:** 0

25 **Number of words for abstract:** 250, **introduction:** 625, **discussion:** 1500

26

27 **Conflict of interest statement:**

28 The authors declare no competing financial conflicts of interest.

29

30 **Acknowledgements:**

31 This work was supported by the National Institutes of Health (Grants K08NS099503,
32 RF1NS124557 to A.S.) and by grants from the Swiss National Science Foundation (project grant
33 310030B_170269 to F.H.; Ambizione grant PZ00P3_209114 to P.R.). This project was supported
34 by the OHSU Advanced Light Microscopy (RRID: SCR_009961) core.

35 **Abstract**

36 Calcium imaging is a key method to record the spiking activity of identified and genetically targeted
37 neurons. However, the observed calcium signals are only an indirect readout of the underlying
38 electrophysiological events (single spikes or bursts of spikes) and require dedicated algorithms to
39 recover the spike rate. These algorithms for spike inference can be optimized using ground truth
40 data from combined electrical and optical recordings, but it is not clear how such optimized
41 algorithms perform on cell types and brain regions for which ground truth does not exist. Here, we
42 use a state-of-the-art algorithm based on supervised deep learning (CASCADE) and a non-
43 supervised algorithm based on non-negative deconvolution (OASIS) to test spike rate inference in
44 spinal cord neurons. To enable these tests, we recorded specific ground truth from glutamatergic
45 and GABAergic somatosensory neurons in the superficial dorsal horn of spinal cord in mice of both
46 sexes. We find that CASCADE and OASIS algorithms that were designed for cortical excitatory
47 neurons generalize well to both spinal cord cell types. However, CASCADE models re-trained on
48 our ground truth further improved the performance, resulting in a more accurate inference of spiking
49 activity from spinal cord neurons. We openly provide re-trained models that can be applied to spinal
50 cord data with variable noise levels and frame rates. Together, our ground-truth recordings and
51 analyses provide a solid foundation for the interpretation of calcium imaging data from spinal cord
52 dorsal horn and showcase how spike rate inference can generalize between different regions of the
53 nervous system.

54 **Significance Statement**

55 Calcium imaging is a powerful method for measuring the activity of genetically identified neurons.
56 However, accurate interpretation of calcium transients depends on having a detailed understanding
57 of how neuronal activity correlates with fluorescence. Such calibration recordings have been
58 performed for cerebral cortex but not yet for most other CNS regions and neuron types. Here, we
59 obtained ground truth data in spinal cord by conducting simultaneous calcium and electrophysiology
60 recordings in excitatory and inhibitory neurons. We systematically investigated the transferability of
61 cortical algorithms to spinal neuron subpopulations and generated inference algorithms optimized to
62 excitatory and inhibitory neurons. Our study provides a foundation for the rigorous interpretation of
63 calcium imaging data from spinal cord.

64 **Introduction**

65 The development of genetically encoded calcium indicators and two-photon microscopy have
66 significantly improved our ability to measure neuronal population dynamics in intact tissues,
67 providing unique insights into brain function over large spatiotemporal scales (Grienberger and
68 Konnerth, 2012; Ji et al., 2016; Nelson et al., 2019). Calcium indicators, e.g., from the GCaMP family
69 (Tian et al., 2009; Chen et al., 2013; Zhang et al., 2023), can be expressed using cell-specific
70 promoters, allowing the characterization of neuronal activity in normal and pathological states in
71 distinct neuronal populations. A fundamental problem remains to infer from the fluorescence signals
72 the underlying neuronal activity, since calcium indicators provide only an indirect measure of
73 neuronal spiking (Kerr et al., 2005; Yaksi and Friedrich, 2006; Lütcke et al., 2010). This is a non-
74 trivial issue, as the relationship between calcium signals and electrophysiological spikes is non-linear
75 and may depend on parameters such as the respective calcium indicator, expression levels, brain

76 areas, cell types, and recording noise. It is therefore not clear whether an algorithm adapted for a
77 specific dataset will generalize well to datasets recorded under different conditions. Optimizing spike
78 inference thus requires not only the development and training of algorithms but also ground truth
79 recordings to re-train and re-evaluate the performance of these algorithms. Such ground truth
80 recordings are experimentally challenging since they require simultaneous electrophysiological
81 recordings and calcium imaging from the same neurons. Most openly accessible ground truth
82 datasets comprise only mouse neocortical neurons, and whether algorithms trained with these
83 datasets can be applied to other neuronal populations, such as in the spinal cord, remains unknown.

84 The spinal cord is a complex structure supporting sensory, motor, and autonomic functions (Häring
85 et al., 2018; Sathyamurthy et al., 2018). Multiple distinct populations exist in the dorsal horn of the
86 spinal cord, broadly divided into excitatory (glutamatergic) and inhibitory (GABAergic) neurons,
87 which can be targeted based on specific promoters (Fan and Sdrulla, 2020; Larsson, 2017; Todd,
88 2017). These populations receive and integrate somatosensory afferents and play critical roles in
89 disease states such as pathological pain and itch (Christensen et al., 2016; Koch et al., 2018;
90 Moehring et al., 2018; Peirs et al., 2020; Sullivan and Sdrulla, 2022). Importantly, they reside in the
91 superficial laminae of the dorsal horn and therefore are accessible for two-photon imaging
92 (Johannssen and Helmchen, 2013; Xu and Dong, 2019; Harding et al., 2020b).

93 Two-photon imaging of the spinal cord in the living animal is well established (Kerschensteiner et al.,
94 2005; Misgeld et al., 2007; Drdla et al., 2009; Johannssen and Helmchen, 2010; Dibaj et al., 2010;
95 Farrar et al., 2012; Ran et al., 2016), but the degraded visual accessibility due to heavily myelinated
96 tissue together with motion artifacts pose major challenges (Davalos et al., 2008; Laffray et al., 2011;
97 Nishida et al., 2014; Sekiguchi et al., 2016). Partly because of this reduced accessibility, only very
98 few calcium recordings have been performed in conjunction with simultaneous electrophysiology
99 (Harding et al., 2020a). A small number of studies have been performed to study the specific role of
100 calcium signaling in spinal cord neurons (Harding et al., 2020a; Simonetti et al., 2013) but there are,
101 to our best knowledge, no attempts to systematically calibrate calcium signals of spinal cord neurons
102 for spike inference. This is problematic because spinal cord neurons differ from cortical neurons in
103 their development and function, and it is therefore unclear how spike inference and calibration
104 measurements from cortical calcium signals can be applied to spinal cord neurons.

105 Here, we conducted simultaneous cell-attached recordings and calcium imaging of dorsal horn
106 neurons to study the relationship between calcium signals and electrophysiological action potentials.
107 With this ground truth, we can systematically evaluate and re-train algorithms for spike rate
108 inference, enabling a better-founded interpretation of calcium imaging data from spinal cord in the
109 future.

111 **Materials and Methods**

112 **Mouse Strains**

114 VGlut2-Cre mice (Stock No: 016963, The Jackson Laboratory) were crossed with homozygous floxed GCaMP6s mice
115 (derived from strain Ai96; Stock No: 024106, The Jackson Laboratory, Bar Harbor, ME), resulting in GCaMP6s expression
116 in glutamatergic neurons. To drive expression of GCaMP6s in GABAergic interneurons, we crossed *Viaat-Cre* mice (Stock
117 No: 016962, The Jackson Laboratory) with homozygous GCaMP6s mice. The mice were kept under standard colony

118 conditions, with 12-hour day/night cycles, and had access to food and water ad libitum. Both males and females were
119 used. All experiments were approved by the Institutional Animal Care and Use Committee at Oregon Health & Science
120 University.

121

122 **Ex vivo lumbar spinal cord preparation**

123 Four- to six-week-old *Viaat*/GCaMP6s or *VGlut2*/GCaMP6s mice of both sexes were deeply anesthetized with 5%
124 isoflurane and decapitated. The lumbar spinal cord was rapidly removed *en bloc* and placed in oxygenated artificial
125 cerebrospinal fluid (ACSF; in mM: 125 NaCl, 2.5 KCl, 26 NaHCO₃, 1.25 NaH₂PO₄H₂O, 1 MgCl₂, 2 CaCl₂, and 25 glucose)
126 at room temperature. The dorsal roots were trimmed, and the dura was removed. During experiments, the tissue block
127 was glued to a thick glass rectangle and perfused with room-temperature, oxygenated ACSF at 3 mL/min. In a subset of
128 experiments (5 out of 21 recordings in *VGlut2* mice), ACSF was warmed to physiological temperatures (37°C) to test for
129 the effect of temperature on calcium indicator kinetics.

130 **Calcium imaging acquisition**

131 For calcium imaging of spinal cord neurons *ex vivo* or *in vivo*, the imaging system consisted of a Zeiss 7 MP microscope
132 (Zeiss Instruments, Thornwood, NY) equipped with a femtosecond-pulsed tunable Ti:Sapphire laser (Coherent, Santa
133 Clara, CA), tuned to a wavelength of 940 nm (<40 mW at back aperture). Fluorescence images were acquired using a
134 20X/1.0 water immersion objective. GCaMP6s signal was filtered through a green pass band filter (500-550 nm), while red
135 pipette fluorescence was filtered through a 575-610 nm band filter. Fluorescence images were acquired at either low
136 (~2.5 Hz) or high (>30 Hz) imaging rate for ground truth recordings *ex vivo* (Table 1) and at ~3 Hz *in vivo*.

137 **Electrophysiological recordings**

138 For ground truth recordings, calcium imaging was performed as described above together with electrophysiological
139 recordings of the same neuron. Superficial dorsal horn neurons with spontaneous or dorsal root-evoked activity were
140 identified and targeted for cell-attached recording. A pipette microelectrode was pulled from borosilicate glass capillaries
141 (B150F-4, World Precision Instruments, Sarasota, FL) with the Model P-97 micropipette puller (Sutter Instrument, One
142 Digital Drive, Novato, CA) to achieve a tip resistance of ~4-6 MΩ. The pipette was filled with ACSF containing 30 μM CF594
143 (Sigma-Aldrich) filtered with a 0.22 μm filter and mounted on an MP-225 motorized micromanipulator (Sutter Instrument).
144 Positive pressure was applied, and the pipette tip was guided into the dorsal horn using the two-photon microscope by
145 switching between the green (for GCaMP) and red (for CF594) channels to approach the target neuron. Then, pressure
146 was released, and a small amount of negative pressure was used to attach to the membrane. Extracellular action potentials
147 were amplified with a differential amplifier (Model 3000, A-M Systems, Sequim, WA). Signals were high-pass filtered at
148 300 Hz and low-pass at 10 kHz. They were sampled at 10 kHz with Digidata1440A and recorded with Clampex 10.7
149 (Molecular Device/Axon Instruments, San Jose, CA). The *ex vivo* preparation cannot cover natural responses to external
150 input due to the severed connections to ascending and descending pathways. We therefore used dorsal root stimulation
151 to increase the spectrum of neuronal activity covered by our ground truth recordings. Dorsal root stimulation was delivered,
152 as described previously (Fan et al., 2022), via a tight-fitting, thin-wall glass pipette (1.2 mm diameter; Sutter Instruments,
153 Novato, CA) backfilled with ACSF and attached to the root via suction, typically at L4. Dorsal root stimulation consisted of
154 a square pulse (0.2 ms duration), 500 μA intensity. Stimulation was delivered using a stimulus isolator (A365, WPI,
155 Sarasota, FL) driven by a waveform generator (Pulsemaster A300, WPI). On average, neurons received 3.0 [0.0-5.5]
156 stimulations (median with interquartile range across neurons), corresponding to one stimulation every 135 s on average.
157 GABAergic neurons were stimulated more frequently than glutamatergic neurons (1.0 [0.0-2.3] stimulations for
158 glutamatergic and 4.0 [3.0-7.5] for GABAergic neurons). For both datasets, these statistics include neurons that were not
159 stimulated at all. All stimulation responses were also included to train CASCADE models in order to make CASCADE
160 robust towards such evoked activity patterns. Furthermore, our publicly available ground truth datasets acquired for spinal
161 cord (<https://github.com/HelmchenLabSoftware/Cascade>) contains not only spike times but also the time points of dorsal
162 root stimulation for each recording.

163 **In vivo lumbar spinal cord calcium imaging**

164 To apply spike rate inference to *in vivo* data, we used previously acquired calcium imaging datasets that were based on
165 an imaging window above the lumbar spinal cord (modified from (Farrar et al., 2012)) and that targeted the same two
166 classes of neurons as in ground truth recordings (Sullivan and Sdrulla, 2022). All experiments were acquired at ~3 frames
167 per second with the same two-photon microscope used for *ex vivo* imaging experiments. Anesthetic experiments were
168 carried out by exposing mice to 1% isoflurane for at least 10 minutes prior to 5-minute recordings of activity under this
169 condition. The isoflurane concentration was then increased to 2% and the same incubation and recording periods ensued.

170 **Extraction of simultaneous calcium imaging and electrophysiology recordings**

171 For calcium imaging movies, recorded neurons were outlined in ImageJ, and the raw fluorescence was averaged for each
172 region of interest. $\Delta F/F_0$ was calculated with F_0 being the 10th percentile of raw fluorescence values. For
173 electrophysiological recordings, action potentials were detected using a threshold to extract an initial template for refined
174 matching based on the generated template (Pernía-Andrade et al., 2012), followed by visual inspection of all detected
175 action potentials, as described before (Rupprecht et al., 2021). Electrophysiological and extracted $\Delta F/F_0$ were aligned
176 using time stamps at the beginning and end of each recording. The extracted ground truth datasets are available online
177 together with existing ground truth datasets in a format that can be accessed both in MATLAB and Python (datasets DS#40
178 and DS#41 on <https://github.com/HelmchenLabSoftware/Cascade>).

179 **Extraction of neuronal traces from in vivo recordings**

180 Calcium imaging movies were processed with non-rigid motion correction (Pnevmatikakis and Giovannucci, 2017). Next,
181 neuronal ROIs were extracted manually based on their anatomy and based on their functional response using the map of
182 local correlations with an interactive user interface as described previously (Rupprecht and Friedrich, 2018). From the
183 extracted raw ROI traces, $\Delta F/F_0$ was computed with the baseline level F_0 defined as the 10th percentile of fluorescence
184 values. To infer spike rates from $\Delta F/F_0$ traces, we applied CASCADE models trained on ex vivo glutamatergic and
185 GABAergic spinal cord neurons (available as *Spinal_cord_inhibitory_3Hz_smoothing400ms_high_noise* and
186 *Spinal_cord_excitatory_3Hz_smoothing400ms_high_noise* via <https://github.com/HelmchenLabSoftware/Cascade>).

187 **The mouse cortex dataset**

188 For the 'cortex dataset', fluorescence traces were downloaded from <https://portal.brain-map.org/explore/circuits/oephys>,
189 extracted and processed as described before (Rupprecht et al., 2021). The data consist of neuronal ground truth recordings
190 in cortical layer 2/3 during anesthesia from four transgenic mouse lines that express in specific cortical excitatory
191 subpopulations (Huang et al., 2021). Recordings include periods without and with visual stimulation using static and drifting
192 gratings. Neuropil correction (neuropil contamination ratio, 0.7) was performed and $\Delta F/F_0$ was computed using a 6-s
193 running 10th percentile window (adjusted to the noisiness of each recording). Importantly, ground truth recordings were
194 carefully quality-controlled as described (Rupprecht et al., 2021).

195 **Extraction of the calcium response for the average action potential**

196 The calcium response for the average action potential for each neuron (*i.e.*, the linear kernel; Fig. 3a) was extracted by
197 regularized deconvolution using the *deconvreg(calcium,spikes)* function in MATLAB (MathWorks). This function computes
198 the kernel, which, when convolved with the observed *spikes*, results in the best approximation of the *calcium* trace. The
199 same linear kernel was used for the linear forward model to predict the linear expected response (Fig. 3e).

200 **Computation of noise levels**

201 Standardized noise levels were computed, as described previously in more detail (Rupprecht et al., 2021), as the median
202 absolute fluctuations of $\Delta F/F$ between adjacent timepoints, normalized by the square root of the imaging frame rate f_r :

$$204 \quad v = \frac{\text{Median}_t |\Delta F/F_{t+1} - \Delta F/F_t|}{\sqrt{f_r}}$$

205 When computed for $\Delta F/F$ data, v is quantitatively comparable across datasets, even when frame rates differ, hence the
206 name "standardized noise levels". The units for v are $\% \cdot \text{Hz}^{-1/2}$, which we omit in the main text for readability.

207 **Quantification of spike rate inference performance**

208 Ground truth spike rates used for training and evaluation were generated from discrete ground truth spikes by convolution
209 with a Gaussian smoothing kernel. To take advantage for the respective sampling rate, the precision of the ground truth
210 was adjusted by tuning the standard deviation of the smoothing Gaussian to the temporal sampling rate ($\sigma = 0.4$ s for 2.5-
211 Hz recordings, $\sigma = 0.2$ s for 5 Hz, $\sigma = 0.1$ s for 10 Hz, $\sigma = 0.1$ s for 15 Hz, $\sigma = 0.1$ s for 20 Hz, $\sigma = 0.05$ s for 25 Hz and
212 $\sigma = 0.05$ s for 30 Hz recordings unless otherwise stated). This smoothed ground truth spike rate was then compared to the
213 inferred spike rate.

214 To generate ground truth at specific frame rates and noise levels from the existing ground truth, $\Delta F/F$ traces were temporally
215 resampled and Gaussian noise was added until the desired noise level was reached, as described previously (Rupprecht
216 et al., 2021). Therefore, for a given condition (e.g., standardized noise level of "7" and sampling rate of 30 Hz), ground
217 truth from a neuron recorded at a standardized noise level larger than the desired level or at an imaging rate slower than

218 the desired sampling rate was used. This procedure enabled the consistent evaluation of algorithms across datasets and
219 individual neurons for standardized ground truth at specific frame rates and noise levels.

220 **Spike rate inference with CASCADE and OASIS**

221 For spike rate inference with OASIS, the Python implementation of the algorithm in Suite2p (Pachitariu et al., 2019) was
222 downloaded from <https://github.com/MouseLand/suite2p> and used in Python 3.9 with default parameters. For evaluation
223 of spike rate inference results with OASIS, we tested Gaussian smoothing kernels of variable standard deviation and
224 temporal shifts between -1 and +1 s to find the amount of smoothing and the delay for each dataset that optimized the
225 correlation with ground truth. For spike rate inference with “default CASCADE”, pretrained models together with the
226 algorithm were downloaded from <https://github.com/HelmchenLabSoftware/Cascade>. These models had been trained on
227 a large database of excitatory neurons across different brain areas but focused on cortical recordings (“global models” in
228 CASCADE). Within this study, these models are called “default CASCADE” because they were not retrained with ground
229 truth acquired from spinal cord.

230 **Retraining CASCADE for spike rate inference with spinal cord neurons**

231 CASCADE was retrained from scratch on spinal cord ground truth with the same procedures as described before
232 (Rupprecht et al., 2021). The retrained CASCADE networks consist of a standard convolutional network with six hidden
233 layers, including three convolutional layers. The input consists of a window of 64 time points (32 time points for frame rates
234 <15 Hz), symmetric around the time point for which the inference was made. The three convolutional layers have relatively
235 large filter sizes (31, 19 and 5 time points; 17, 9 and 3 time points for frame rates <15 Hz), with an increasing number of
236 features (20, 30 and 40 filters per layer), with max pooling layers after the second and third layer, and a densely connected
237 hidden layer consisting of ten neurons as the final layer. Models for spinal cord neurons were trained separately on
238 glutamatergic and GABAergic neurons, including all available neurons, except for GABAergic neurons with extremely high
239 outlier spike rates that would otherwise strongly bias the training. Care was taken not to use the same neuron for training
240 and testing of a model. For example, if a model trained at a frame rate of 30 Hz with the glutamatergic dataset was tested
241 on glutamatergic neurons, a new model was trained for each test neuron on all glutamatergic spinal cord neurons except
242 the neuron tested for (“leave-one-out” strategy). This strategy of cross-validation prevents fitting of test data and enables
243 us to test the generalization of the algorithm to unseen data. Models retrained with spinal cord data are already integrated
244 into CASCADE (<https://github.com/HelmchenLabSoftware/Cascade>) for a subset of sampling rates (2.5 Hz, 3 Hz and
245 30 Hz); further models tailored towards special use cases can be readily requested as described on this Github page.

246 **High-frequency spike events**

247 For the analysis of short events with a large number of spikes (“high-frequency spike events”; Fig. 5), we used the selection
248 criterion that the maximum instantaneous spike rate of the ground truth exceeded 45 Hz. Changes to the threshold resulted
249 in qualitatively similar results.

250 **Experimental design and statistical analysis**

251 The number of recorded ground truth neurons (approx. 20 per group) was similar to previous studies that analyzed such
252 ground truth recordings (Tian et al., 2009; Chen et al., 2013; Huang et al., 2021). The animal’s sex was not included as
253 analysis variable due to the limited sample size. Statistical analyses were performed in MATLAB 2020a. Only non-
254 parametric tests were used. The Mann–Whitney rank-sum test was used for non-paired samples, and the Wilcoxon signed-
255 rank test was used for paired samples. Two-sided tests were applied unless otherwise stated. Box plots used standard
256 settings in MATLAB, with the central line at the median of the distribution, the box at the 25th and 75th percentiles and the
257 whiskers at extreme values excluding outliers (outliers defined as data points that are more than 1.5·D away from the 25th
258 or 75th percentile value, with D being the distance between the 25th and 75th percentiles).

259 **Software Accessibility**

260 CASCADE software, together with CASCADE models trained on glutamatergic or GABAergic spinal cord ground truth and
261 the ground truth datasets are available online via <https://github.com/HelmchenLabSoftware/Cascade>.

262 Results

263 Ground truth recordings for calcium imaging in mouse spinal cord

264 To understand how calcium signals in spinal cord neurons relate to the underlying action potentials
265 and how this relationship might differ between excitatory and inhibitory cells, we performed
266 simultaneous electrophysiological recordings and calcium imaging in the intact, ex vivo spinal cord
267 isolated from transgenic mice expressing GCaMP6s either in vGluT2- (glutamatergic) or vIAAT-
268 positive (GABAergic) cells (Fan et al., 2022) (Fig. 1a,b; Methods). Cell-attached electrical recordings
269 were established on individual GCaMP6s-expressing neurons, as identified under the two-photon
270 microscope, permitting the simultaneous recording of action potentials (spikes) and calcium signals
271 from the same cell (Fig. 1c-d). We recorded from 21 glutamatergic and 23 GABAergic neurons and
272 collected ground truth data with >70 000 action potentials over a total recording duration of 7.4 hours.
273 Recordings were performed in two imaging configurations, either acquiring movies with a field-of-
274 view (FOV) used for population imaging (512^2 pixels; approx. $425\ \mu\text{m}$ side length) at a low frame
275 rate of approximately 2.5 Hz (Fig. 1c,d), or with a smaller imaging FOV ($35^2 - 45^2$ pixel, approx. 30-
276 $35\ \mu\text{m}$ side length) at a higher frame rate (33 ± 8 Hz, mean \pm s.d.; inset in Fig. 1c,d). The
277 simultaneously performed electrophysiological recordings exhibited a broad diversity of spiking and
278 bursting patterns, with variable spike rates (SR) between as well as within excitatory and inhibitory
279 cell types (Fig. 1e-j). More details about the summary recording statistics are provided in Table 1.

280 Variability of spike patterns across neurons and datasets

281 First, we systematically analyzed the spike patterns for glutamatergic and GABAergic spinal cord
282 neurons from the ground truth recordings and compared the results with previously obtained ground
283 truth datasets from GCaMP-expressing mouse cortical neurons, hence called the 'cortex dataset'
284 (Huang et al., 2021). This cortex dataset consists of ground truth recordings from 80 neurons in
285 animals with four different transgenic strategies to express either GCaMP6s or GCaMP6f in layer
286 2/3 pyramidal cells of visual cortex (Fig. 1-1 for examples of recordings) (Huang et al., 2021).

287 For spinal cord ground truth recordings, we observed that spike rates varied by an order of magnitude
288 within both the glutamatergic and the GABAergic spinal cord dataset (Fig. 2a). Spike rates of
289 glutamatergic neurons in these recordings were, on average, significantly higher compared to
290 GABAergic neurons ($p = 0.001$, both when including only spontaneous activity periods or also
291 stimulation periods; Wilcoxon rank sum test) and distributed more uniformly across a broader range
292 (Fig. 2a; but notice the outlier GABAergic neuron with very high spike rate).

293 The relationship between neuronal spiking and the observed fluorescence signal from calcium
294 indicators is typically non-linear. For example, it is possible that a neuron exhibits no discernible
295 calcium response to a single spike but a strong calcium response to two or three closely spaced
296 spikes. Therefore, the electrophysiological spike patterns of a neuron will influence how well
297 information about spikes can be extracted from calcium imaging data. We thus investigated the
298 bursting propensity of the recorded spinal neurons and compared it to existing cortical datasets. To
299 this end, we went through all spikes recorded for a given neuron and measured the temporal distance

300 between each spike and its closest neighboring spike. This procedure is similar to the computation
301 of inter-spike intervals but searches for the closest neighboring spike in either the past or future and
302 therefore measures more accurately whether a given spike is part of a burst or not. Then, we plotted
303 the cumulative distribution of closest temporal neighbors for each neuron (Fig. 2b). Based on this
304 analysis, we found that the bursting propensity (defined here as the fraction of spikes that were within
305 10 ms of any neighbouring spike) was highest for the neurons in the cortex dataset ($42 \pm 23\%$,
306 median \pm s.d. across neurons), followed by the glutamatergic ($16 \pm 33\%$) and the GABAergic
307 ($6.5 \pm 8.0\%$) spinal cord neuron datasets. This result was supported by a complimentary analysis
308 measuring the coefficient of variation (COV) of inter-spike intervals as a standard measure of
309 burstiness (Softky and Koch, 1993) (Fig. 2c), displaying a marked increase of the COV for the cortex
310 dataset compared to the spinal cord datasets ($p < 10^{-6}$) but no difference between the excitatory and
311 inhibitory spinal cord datasets ($p = 0.24$). These findings also held true when analyzing only
312 spontaneous activity periods for spinal cord recordings (Fig. 2c). These analyses reveal that
313 glutamatergic and particularly GABAergic neurons recorded in our spinal cord ground truth exhibited
314 less bursty firing patterns than neurons from the cortex dataset but rather fired more steadily and
315 regularly as indicated by the COV. These differences between spinal cord and cortical recordings
316 may also be explained by different recording conditions (ex vivo vs. anesthetized). However, the
317 burstiness of cortical pyramidal neurons is a well-studied phenomenon that is observed both in vivo
318 and ex vivo (Friedenberger et al., 2023), suggesting that the reduced burstiness of spinal cord
319 neurons is also likely to be conserved across conditions. These analyses further emphasize the
320 issue of how well algorithms for spike rate inference generalize across such differences.

321 **Magnitude and variability of spike-evoked calcium signals**

322 Next, we examined the variability of the evoked calcium signals in response to a well-defined
323 electrophysiological event (Fig. 3a-c). To this end, we took advantage of the fact that calcium signals
324 can be approximated as a convolution of spikes with a kernel function (*i.e.*, the calcium response
325 evoked by the average spike). The kernel can be easily retrieved from the ground truth by
326 deconvolution of the recorded calcium signals ($\Delta F/F$) with the simultaneously recorded spikes, as
327 shown before (Rupprecht et al., 2021). The kernel therefore constitutes the $\Delta F/F$ response not to
328 isolated spikes but to the average spike. We found that the resulting calcium response kernels for
329 both glutamatergic and GABAergic spinal cord neurons exhibited visibly slower time courses
330 compared to previously performed recordings in mouse cortex with GCaMP6s and GCaMP6f (Huang
331 et al., 2021) (single-exponential fits for the time constant τ yielded 3.1 ± 0.5 s, fit $\pm 90\%$ confidence
332 interval, for glutamatergic spinal cord neurons; 4.4 ± 0.7 s for GABAergic neurons; 0.8 ± 0.1 s for the
333 cortex dataset). In a subset of recordings, we performed physiological (37°C) instead of room
334 temperature recordings but did not observe a visibly faster calcium response function (Fig. 2-1;
335 $\tau = 2.9 \pm 0.5$ s for room temperature, 3.0 ± 0.6 s for physiological temperature). For the response
336 kernel amplitudes as measured by peak response (maximum $\Delta F/F$) and mean response (average
337 $\Delta F/F$ during the 2 s post-event window), we observed a striking variability on a neuron-to-neuron
338 basis for spinal cord datasets (Fig. 3b,c; blue and red) and the mouse cortex dataset (Fig. 3b,c;
339 black). This is consistent with the previously found variability of response amplitudes from neuron to

340 neuron (Éltes et al., 2019; Rupprecht et al., 2021). The response magnitude was consistent with
341 previous similar analyses (Rupprecht et al., 2021). We wondered whether the response kernel could
342 be distorted by the inclusion of dorsal root stimulations, because such stimulations might recruit
343 slowly acting neuromodulators (Geppetti et al., 2015; Todd and Spike, 1993) that may influence
344 intracellular calcium (Warwick et al., 2022); alternatively, stimulation may lead to bursts and
345 prolonged membrane depolarizations in the recorded neuron, events that have been associated with
346 prominent calcium signals (Ledochowitsch et al., 2020; Milicevic et al., 2024). However, we did not
347 observe a striking difference when including the stimulation periods (average response as in Fig. 3b,
348 median \pm s.d., $12 \pm 6\%$ and $11 \pm 7\%$, for glutamatergic and GABAergic neurons) and when
349 excluding the stimulation periods ($12 \pm 7\%$ and $11 \pm 8\%$), indicating that dorsal root stimulation did
350 not elicit responses distinct from spontaneous activity.

351 The average peak response of a subset of neurons surpassed the typical levels of $\Delta F/F$ fluctuations,
352 but for the large fraction of neurons this was not the case (Fig. 3c). From a simulation based on linear
353 convolution of calcium kernels with realistic noise levels (Fig. 3d), calcium responses cannot be
354 visually discerned for <2 -4 quasi-simultaneous spikes for low-noise recordings (standardized noise
355 level of 1.0, as defined in Methods, frame rate of 40 Hz) and for <4 spikes for high-noise recordings
356 (noise level of 5.0, frame rate of 2.5 Hz). The real response to isolated single spikes might be even
357 smaller due to the known sigmoid non-linearity of GCaMP6 (Rose et al., 2014).

358 Finally, we attempted to visualize the linearity of the calcium indicator responses to spike rates for
359 each dataset. In principle, the same indicators should yield a similar calcium vs. fluorescence
360 relationship across cells, but only if the respective intracellular calcium ranges are comparable.
361 However, due to the variability of typical calcium concentrations across cell types (Maravall et al.,
362 2000) and the sigmoid calcium concentration response curve of GCaMPs (Rose et al., 2014), the
363 same indicator might behave linearly in one condition, supra-linearly in another and saturating in yet
364 another. A typical method to quantify linearity is to measure responses evoked by a set of one, two
365 or more isolated action potentials (Kerr et al., 2005; Lütcke et al., 2010). However, in our recorded
366 spinal cord ground truth dataset, isolated singlets, doublets or triplets of action potentials occurred
367 only in few neurons, therefore disabling this approach. Instead, we computed the expected
368 fluorescence response from the measured spike pattern as estimated with a linear spike-to-calcium
369 forward model (Wei et al., 2020). In this forward model, we employed linear convolution of the spike
370 pattern with the calcium response kernel as computed before (Fig. 3a). We observed that the
371 experimentally measured $\Delta F/F$ was reasonably linear according to such a forward model for
372 GABAergic spinal cord neurons and, to a lesser extent, for glutamatergic spinal cord neurons
373 (Fig. 3e). In contrast, such a linear relationship was less obvious in the cortex dataset (Fig. 3e). This
374 qualitative finding shows that the experimentally measured $\Delta F/F$ reflects changes of the gradually
375 and slowly changing underlying spike rates in most of the ground truth recordings in spinal cord (see
376 also Fig. 1e,f,g,i,j). This result is reminiscent of observations made for cortical interneurons (Inoue
377 et al., 2019; Kwan and Dan, 2012) but in contrast to the cortex datasets from excitatory neurons, in
378 which isolated calcium transients due to bursts (Fig. 2b,c) rather than regular firing were typically
379 observed (Chen et al., 2013; Huang et al., 2021). This finding of gradually and relatively linearly

380 changing fluorescence suggests that raw $\Delta F/F$ might be considered as a useful approximation of
381 spike rates for spinal cord neurons without any spike inference algorithm applied.

382 **Spike rate inference from spinal cord calcium imaging data**

383 Next, we wanted to benchmark methods to infer spiking activity from calcium imaging data in spinal
384 cord. To address this challenge, we used several complementary approaches (Fig. 4a). First,
385 following up on our investigation of calcium response linearity, we used the raw $\Delta F/F$ signal as a
386 proxy for spiking activity. Second, we used OASIS, an unsupervised spike rate inference algorithm
387 based on non-negative deconvolution that is used as default option in the two most widely employed
388 toolboxes for source extraction of calcium imaging data (CalmAn, Suite2p) (Giovannucci et al., 2019;
389 Pachitariu et al., 2019). Third, we used a supervised spike rate inference algorithm (CASCADE)
390 trained on a diverse and large dataset that mostly contained recordings from mouse cortex and no
391 neurons from spinal cord (Rupprecht et al., 2021). Finally, we retrained CASCADE on our specifically
392 recorded ground truth spinal cord datasets containing either glutamatergic or GABAergic neurons.
393 Among these algorithms, only the CASCADE models provide an estimate of absolute spike rates.
394 Importantly, to test these retrained supervised CASCADE models on our spinal data sets, we applied
395 a “leave-one-out” principle, where CASCADE was retrained each time with the “test neuron”
396 excluded. This procedure enabled us to test the generalization of the algorithm without reducing the
397 dataset. To standardize the benchmarking, we used experimentally recorded datasets but for each
398 recording added Gaussian noise until a certain ‘standardized noise level’ (e.g., a noise level of “7”
399 (Methods) was reached. Similarly, we used downsampling of recorded data to generate a
400 benchmarking dataset of a specified frame rate (e.g., 30 Hz). This procedure, as introduced
401 previously (Rupprecht et al., 2021), standardizes performance evaluations and makes them
402 comparable across neurons within datasets and across datasets.

403 To compare these approaches, we performed spike rate inference for all recorded neurons in our
404 two ground truth datasets. As an initial result of our comparison, all algorithms performed reasonably
405 well and yielded meaningful predictions (Fig. 4b-c; Fig. 4-1).

406 To quantify the performance of each approach, we computed the correlation between predicted and
407 true spike rates as done previously (Berens et al., 2018; Rupprecht et al., 2021; Theis et al., 2016).
408 Such a performance metric, however, puts the $\Delta F/F$ approach at a disadvantage since $\Delta F/F$ will
409 always be delayed with respect to the spiking ground truth, thereby reducing the correlation with
410 ground truth. A similar systematic delay was also found for model-based spike rate inference
411 algorithms like OASIS in a previous study (Rupprecht et al., 2021). We, therefore, shifted the
412 predictions temporally to optimize the correlation with the same shift applied to all neurons of a given
413 dataset (Fig. 4-2) and used this optimal temporal shift to evaluate a given dataset and approach to
414 estimate spiking activity.

415 We quantified performance using a fixed sampling frequency (30 Hz) and a fixed noise level of the
416 calcium imaging data. For these fixed settings, typical correlation values as a performance readout
417 (median value across all spinal cord neurons) were ~ 0.25 $\Delta F/F$, ~ 0.30 for OASIS and ~ 0.47 for
418 default CASCADE. Predictions using default CASCADE were overall better than predictions by

419 OASIS or when using $\Delta F/F$ as a direct proxy, and this finding held true both for the glutamatergic
420 and GABAergic dataset (Fig. 4d,e; median correlation of $0.p < 0.001$ for all comparisons; Wilcoxon
421 signed-rank test; $n = 23$ and 21 neurons for the glutamatergic and GABAergic dataset). In addition,
422 we found that a version of CASCADE that was retrained with a specific dataset (sticking to the “leave-
423 one-out” principle) performed equally or slightly better than the default CASCADE algorithm (p-value
424 $p = 0.37$, increase of median performance $\Delta r = -3.4\%$ for the glutamatergic dataset; $p = 0.001$,
425 $\Delta r = +8.3\%$ for the GABAergic dataset), and slightly better than the same algorithm trained with the
426 other spinal cord dataset ($p = 0.0057$, $\Delta r = +9.1\%$, and $p = 0.0006$, $\Delta r = +23.4\%$ for glutamatergic
427 and GABAergic dataset, respectively). In addition, we applied all models to the mouse cortex dataset
428 (Fig. 4f) and found that models designed for cortex performed best with default CASCADE,
429 significantly better than all other tested approaches ($p < 10^{-10}$, signed-rank test, $n = 80$ neurons),
430 followed by OASIS that performed better than CASCADE trained on GABAergic ($p < 10^{-10}$) but not
431 significantly better than CASCADE trained on glutamatergic ground truth ($p > 0.05$). In addition, we
432 tested whether performance improvements through retraining of CASCADE were stronger for
433 potential subtypes of spinal cord neurons as identified for example by mean firing rates or burstiness,
434 but we did not find such a relationship (Fig. 4-4). These analyses show that models not specifically
435 trained for the new datasets generalize reasonably well between cortical and spinal cord data and
436 that retraining improved the performance, in particular for the GABAergic spinal cord neurons.

437 These model performances were confirmed across imaging conditions when re-sampling the ground
438 truth dataset at different imaging rates (Fig. 4g; Fig. 4-3a) and across different resampled noise
439 levels (Fig. 4h; Fig. 4-3b). Notably, the performances of all approaches, including the use of raw
440 $\Delta F/F$, although still distinct from each other, were getting closer for very low imaging rates (2.5 Hz;
441 Fig. 4g and Fig. 4-3a). It should be noted that lower imaging rates were accompanied by lower
442 precision of temporal evaluation (e.g., 400-ms standard deviation Gaussian smoothing for 2.5 Hz
443 imaging rate, and 50-ms standard deviation Gaussian smoothing for 30 Hz imaging rate). As
444 temporal precision was decreased, the performance of the $\Delta F/F$ approach for 30-Hz image rate again
445 came closer to the performance of supervised CASCADE (Fig. 4-3c).

446 Together, these results show that spike rate inference with the supervised CASCADE retrained on
447 a specific dataset outperforms the non-supervised approaches (raw $\Delta F/F$ or OASIS). Only for low
448 calcium imaging rates ($\ll 5$ Hz), the performance of the approach using raw $\Delta F/F$ or OASIS was
449 almost equally good as the retrained supervised algorithm. Furthermore, a default CASCADE
450 algorithm trained on a diverse dataset that does not include spinal cord neurons already performed
451 excellently and could also be used as a reliable spike rate inference algorithm for both glutamatergic
452 and GABAergic neurons in the spinal cord.

453 **Reduced spike rate inference performance on high-frequency spike events**

454 Next, we evaluated the performance of the spike rate inference algorithms across different spike
455 patterns. This evaluation was performed at fixed conditions across neurons and datasets (resampled
456 frame rate of 30 Hz, standardized noise level of 7). From an inspection of predicted spike patterns
457 (Fig. 4c), we noticed that events with a large number of spikes in a small time window, hence called

458 high-frequency spike events, were not well recovered by the algorithms designed for or trained with
459 cortical excitatory neurons, *i.e.*, OASIS or default CASCADE. Specifically, the recovered spike
460 pattern was considerably prolonged compared to the ground truth (Fig. 4c). To quantify this
461 observation, we selected all events where spike rates exceeded a predefined threshold
462 (instantaneous firing rate of 45 Hz, see Methods) (Fig. 5a,f) and plotted the associated $\Delta F/F$ values
463 (Fig. 5b,g), the spike rates inferred by default CASCADE (Fig. 5c,h), by retrained CASCADE
464 (Fig. 5d,i) and by OASIS (Fig. 5e,j). We noticed that spike rates inferred by default CASCADE and
465 even more by OASIS exhibited false positive spike detections when the true spike rate had already
466 decayed (Fig. 5a-j; Fig. 5-1). For retrained CASCADE, the inferred spike rate more accurately
467 reflected the ground truth spike rate dynamics around high-frequency spike events (Fig. 5f,i; Fig. 5-
468 1), demonstrating how spike rate inference for spinal cord neurons can be optimized by retraining.

469 Next, we quantified the accuracy of spike rate inference during these high-frequency spike events.
470 For this comparison, OASIS was not included since the OASIS algorithm is not intended to recover
471 absolute spike rates. We found that spike rates in a 1-s window around high-frequency spike events
472 were systematically underestimated by all versions of CASCADE, probably due to indicator
473 saturation, for both spinal cord ground truth datasets ($p < 0.00002$ for all comparisons; Wilcoxon
474 signed-rank tests across neurons within a dataset; see the absolute values in Fig. 5a,c,f,h and Fig.
475 5-1). However, absolute spike rates were better recovered by retrained CASCADE compared to
476 default CASCADE ($p < 0.00001$ for both the glutamatergic and the GABAergic datasets; Wilcoxon
477 signed-rank tests; Fig. 5c,d,h,i). Hence, spike rates during high spike-rate events were systematically
478 underestimated by spike rate inference, but less so with a retrained supervised algorithm.

479 **Spike rate inference of absolute and relative spike rates**

480 Next, we wanted to quantify how accurately overall spike rates across all event types were reflected
481 by spike rate inference with default or retrained CASCADE. First, we compared absolute spike rates
482 estimated by CASCADE with ground truth spike rates and derived the amount of false positives and
483 false negative detection of spiking activity (Fig. 6a). False positive and negative detections depend
484 on the time window of evaluation because a spike event that is correctly detected but shifted in time
485 will be seen as a false detection if a short time window is used for evaluation but as a correct
486 detection if a longer evaluation time window is applied. Accordingly, false detections decreased when
487 the time window of evaluation was increased and converged towards an average bias for the longest
488 time windows (Fig. 6b,c). We found that default CASCADE resulted in a high fraction of false positive
489 detections for the GABAergic dataset and a high fraction of false negative detections for the
490 glutamatergic dataset. Retraining with specific ground truth (again using the “leave-one-out”
491 strategy) improved upon these problems, as is evident from the quantification (Fig. 6d,c). Therefore,
492 retraining not only improved performance across frame rates and noise levels (Fig. 4) but also
493 reduced the bias of absolute inferred spike rates (Fig. 6a-c).

494 Next, we analyzed how spike rate inference with CASCADE or OASIS improves the estimation of
495 relative spike rates, *i.e.*, the comparison of spike rates, be it across different neurons or for the same
496 neuron across different time windows. To perform this evaluation on the ground truth dataset, we

497 split the recordings into 5-s segments. For each pair of such segments, we evaluated whether the
498 different approaches (raw $\Delta F/F$, OASIS, default CASCADE, retrained CASCADE) correctly identify
499 the segment with the larger number of spikes (Fig. 6d). We performed these analyses first for
500 comparisons of spike rates across neurons, and then for comparisons across 5-s segments within
501 the same neuron.

502 For segment pairs from different neurons (Fig. 6e), the median percentage of correct evaluations
503 was relatively modest for raw $\Delta F/F$ (58% and 67% for the GABAergic and glutamatergic datasets;
504 chance level, 50%), increased modestly after spike rate inference with OASIS (59% and 68%) and
505 default CASCADE (61% and 68%) and further increased for the GABAergic dataset after retraining
506 of CASCADE (63% and 68%; significantly higher than all other approaches for GABAergic neurons,
507 $p < 0.001$; $p < 0.05$ compared with $\Delta F/F$ and $p > 0.05$ compared with OASIS and default CASCADE
508 for glutamatergic neurons; one-sided Wilcoxon signed-rank test). For all approaches, a higher spike
509 rate differences between the two compared segments resulted in a higher percentage of correct
510 evaluations, and this correlation was highest for retrained CASCADE ($r = 0.33 \pm 0.01$, mean \pm s.d.,
511 across 420 neuron-neuron pairs for glutamatergic and 0.39 ± 0.01 across 506 pairs for GABAergic
512 neurons; compared to 0.25 ± 0.01 and 0.30 ± 0.01 for $\Delta F/F$, 0.27 ± 0.01 and 0.33 ± 0.01 for OASIS,
513 0.32 ± 0.01 and 0.34 ± 0.01 for default CASCADE; all p -values < 0.01 for comparisons with retrained
514 CASCADE, one-sided Wilcoxon signed-rank test).

515 Furthermore, we compared segment pairs within the same neuron (Fig. 6f) and observed an overall
516 much higher percentage of correct evaluations already for $\Delta F/F$ (76% and 74% for the GABAergic
517 and glutamatergic datasets), which was further increased after spike rate inference (OASIS: 79%
518 and 75%, default CASCADE: 79% and 77%, retrained CASCADE: 83% and 78%; the latter was
519 significantly higher than all other approaches for GABAergic neurons, $p < 0.0005$; $p > 0.05$ for
520 glutamatergic neurons for all comparisons). Again, the correct percentage correlated positively with
521 the spike rate difference between the two segments, and again this correlation was maximal for
522 retrained CASCADE ($r = 0.25 \pm 0.05$, mean \pm s.d., across 21 glutamatergic and 0.33 ± 0.03 for 23
523 GABAergic neurons; compared to 0.18 ± 0.05 and 0.26 ± 0.03 for $\Delta F/F$, 0.18 ± 0.05 and 0.28 ± 0.03
524 for OASIS, 0.22 ± 0.04 and 0.29 ± 0.03 for default CASCADE; all p -values < 0.05 for comparisons
525 with retrained CASCADE). Therefore, comparisons of spike rates *between* different neurons remain
526 challenging (Fig. 6e), but inference algorithms reliably detect spike rate changes *within* a neuron
527 (Fig. 6f). Nonetheless, spike rate inference, in particular with retrained models, enhanced the
528 statistical power of both comparisons.

529 To further investigate the challenge of comparing inferred spike rates across neurons, we visualized
530 the time-averaged true vs. inferred spike rates per neuron (Fig. 6g), revealing two distinct
531 observations. First, inferred spike rates exhibited lower variability compared to true spike rates in
532 both spinal cord datasets, suggesting that spike inference of calcium imaging data fails to fully
533 capture the true variability of spike rates. This was reflected in a reduced coefficient of variation
534 (CoV), which dropped from 1.53 to 0.20 for GABAergic neurons and from 0.48 to 0.15 for
535 glutamatergic neurons. A similar but smaller reduction was observed in the cortex dataset (CoV:
536 0.84 for true spike rates vs. 0.54 for inferred spike rates). $\Delta F/F$ values showed slightly higher CoV

537 compared to inferred spike rates (0.50, 0.46, and 0.61 for GABAergic, glutamatergic, and cortex
538 datasets, respectively). Second, the differences in true spike rates between neurons did not
539 consistently translate into proportional differences in inferred spike rates (Fig. 6g). We observed an
540 even negative correlation between pairwise true vs. inferred spike rate differences for GABAergic
541 neurons ($c = -0.12$), and only modest correlations for the glutamatergic ($c = 0.46$) and cortex
542 ($c = 0.66$) datasets (Fig. 6h). Interestingly, these positive correlations for glutamatergic and cortex
543 neurons were even more reduced when comparing $\Delta F/F$ differences instead of inferred spike rates
544 ($c = -0.33$ for glutamatergic neurons and $c = 0.44$ for cortical neurons). While the relative variability
545 (CoV) of $\Delta F/F$ was higher and therefore closer to the CoV derived from true spike rates, this variance
546 did not reliably reflect actual differences in spike rates (Fig. 6h) and therefore has to be considered
547 noise. These results indicate that the challenge in comparing spike rates across neurons arises not
548 from spike inference itself but rather from biological variability in calcium signaling across cell types,
549 due to potential differences in calcium buffering, resting calcium levels or spike-evoked transients.
550 The greater diversity of cell types in the spinal cord dorsal horn may explain why these effects appear
551 to be more pronounced in the spinal cord datasets compared to the cortex dataset.

552 **Spike rate inference from anesthetized in vivo spinal cord recordings**

553 Finally, we wanted to test how the CASCADE model retrained on ex vivo spinal cord data transferred
554 to in vivo imaging conditions. To this end, we analyzed previously acquired in vivo spinal cord calcium
555 imaging data from both glutamatergic and GABAergic neurons (Sullivan and Sdrulla, 2022) (Fig. 7a-
556 c). From the extracted $\Delta F/F$ traces of the neuronal populations, we performed spike rate inference
557 with dedicated models retrained for the respective neuronal cell types (Fig. 7d,e). Spike rate
558 inference resulted in denoised recordings, most clearly apparent from the cleaned-up baseline for
559 inferred spiking activity from neurons in phases without activity, as expected from previous
560 applications of CASCADE (Rupprecht et al., 2021). In addition, spike rate inference provided an
561 estimate of the number of spikes during a given event (Fig. 7f-h). The most prominent calcium events
562 of a typical duration of 5 s were estimated to be more than 50 spikes (Fig. 7f,g) or even more than
563 100 spikes, equivalent to a mean spike rate of 10-20 Hz (Fig. 7h). These numbers are consistent
564 with our previous observation that single spikes often evoke undetectable calcium transients;
565 therefore, detectable events are typically associated with a much greater number of spikes (Fig. 3).
566 Furthermore, to test if retrained CASCADE could detect in vivo changes in activity within individual
567 neurons, the level of isoflurane anesthesia was adjusted to either 1% or 2%. As expected, an
568 increase of anesthesia depth substantially decreased the inferred spike rates for the majority of
569 neurons (Fig. 7i). This application showcases that the retrained CASCADE models can be used to
570 provide estimates of spike rates and denoise in vivo recordings.

571

572 **Discussion**

573 In this study, we investigated how information about spike rates can be recovered from calcium
574 imaging data in mouse spinal cord. We recorded ground truth datasets with simultaneous calcium
575 imaging and electrophysiology in genetically identified glutamatergic and GABAergic spinal cord

576 neurons. Based on these datasets, we trained a supervised deep learning algorithm that infers spike
577 rates from calcium imaging data, and we provide these pretrained models in an easy-to-use
578 framework (CASCADE). The original CASCADE model, trained with data from cortical neurons,
579 generalized well to these spinal cord neurons, but specific retraining on spinal cord ground truth
580 improved the retrieval of high-frequency spike events, was less biased in predicting absolute spike
581 rates and resulted in an improved prediction of relative spike rates across and within neurons.

582 Spike inference algorithms can be evaluated based on two qualitatively different outputs, either
583 discrete inferred spike times (Deneux et al., 2016; Hoang et al., 2020; Lütcke et al., 2013; Oñativia
584 et al., 2013; Pnevmatikakis et al., 2016) or continuous and smooth spike rates (Berens et al., 2018;
585 Rupprecht et al., 2021; Theis et al., 2016; Zhou et al., 2023). Here, we only used the latter approach
586 since single spikes cannot be identified under our typical recording conditions (Fig. 3a-d). We used
587 the correlation with true spike rates as main metric and found that supervised spike rate inference
588 with CASCADE yielded substantially better results than spike rate inference with OASIS or by using
589 raw $\Delta F/F$ as a proxy for spiking activity (Fig. 4). This performance gap was reduced when we
590 decreased the temporal precision used to evaluate the algorithms (Fig. 4g; Fig. 4-3c). These
591 analyses indicate that raw $\Delta F/F$ or spike rate inference with OASIS are a good proxy for spiking
592 activity when temporal precision is neglected, while supervised spike rate inference with CASCADE
593 performs well for both low and high temporal precision. Overall, a default version of CASCADE,
594 trained on a large database across diverse brain regions but not including the spinal cord, performed
595 very well on the before unseen spinal cord data. This result highlights the robustness of spike rate
596 inference across CNS regions, and supports previous analyses demonstrating generalization of
597 spike rate inference (Rupprecht et al., 2021).

598 However, we also observed limitations of this capability to generalize to spinal cord data. To improve
599 upon the default algorithm, we performed ground truth recordings in glutamatergic and GABAergic
600 spinal cord neurons. It has been previously shown that a much larger or smaller spike-evoked
601 calcium transient can make it challenging to generalize across datasets, e.g., from excitatory
602 neurons to fast-spiking interneurons (Ali and Kwan, 2020; Rupprecht et al., 2021). Our ground truth
603 recordings show that spike-evoked calcium transients and decay kinetics are, on average, similar
604 between the GABAergic and glutamatergic spinal cord populations (Fig. 3a-c). This is noteworthy
605 since several cortical interneuron types have been shown to exhibit much lower spike-evoked
606 calcium transients than cortical pyramidal cells (Aponte et al., 2008; Kwan and Dan, 2012).

607 In addition, we observe that spike-evoked calcium transients from our spinal cord dataset displayed
608 slower decay times but similar amplitudes compared to recordings from mouse cortex (Fig. 3a). The
609 comparable amplitude lends further support to the transferability of spike rate inference from cortical
610 to spinal cord recordings. It must, however, be kept in mind that our ex vivo ground truth recordings
611 are only an approximation of in vivo conditions, as the spinal cord is resected, perfused with room
612 temperature ACSF and deafferented. Although we did not observe an effect of room vs. physiological
613 temperature recordings on the spike-evoked calcium transient (Fig. 3-1), we cannot exclude potential
614 temperature-related effects with certainty. Furthermore, using the GCaMP signal to target cells for
615 our cell-attached recordings may have introduced a bias toward sampling brightly visible cells, which

616 tend to exhibit higher spontaneous activity. In vivo ground truth recordings in spinal cord are
617 challenging due to the difficulty of access and due to prominent motion artifacts (Johannssen and
618 Helmchen, 2010; Nelson et al., 2019; Sullivan and Sdrulla, 2022). Hence, our ground truth recordings
619 represent a compromise that matches the natural conditions as much as possible. In support of this
620 interpretation, calcium signals of ground truth recordings (Fig. 1) were of similar $\Delta F/F$ amplitude
621 compared to previous in vivo recordings (Sullivan and Sdrulla, 2022), and their spike rates (Fig. 2)
622 were of the same order of magnitude as for electrophysiological recordings (Lucas-Romero et al.,
623 2018) and as the spike rates inferred from anesthetized in vivo recordings (Fig. 7). In addition, spike
624 patterns in our ground truth recordings included both bursts and more regular spiking patterns, in
625 agreement with observations *in vitro* and in vivo across multiple species both for spontaneous and
626 stimulus-evoked patterns (Kumazawa and Perl, 1978; Lucas-Romero et al., 2022, 2018; Medrano et
627 al., 2016; Sandkühler and Eblen-Zajjur, 1994). A caveat to keep in mind are the diverging definitions
628 of specific spike patterns across fields. For example, in this study, we investigated
629 electrophysiologically defined bursts (inter-spike interval <10 ms; Fig. 2), but also high-frequency
630 spike events (peak spike rate of >45 Hz; Fig. 5). These event types overlap but do not coincide with
631 the definition of “bursty” spike patterns used in previous spinal cord studies (Lucas-Romero et al.,
632 2022, 2018). Irrespective of these definitions, our dataset ($>70,000$ spikes over 7.4 hours) includes
633 a diversity of firing patterns and is therefore the best available dataset to train a supervised spike
634 inference algorithm for spinal cord neurons.

635 In general, retraining a supervised spike inference algorithm with a specific ground truth dataset can
636 enable more precise interpretations of population imaging data. Here, we found that spike rate
637 inference with a retrained version of CASCADE was improved compared to OASIS but also
638 compared to default CASCADE (Fig. 4). Interestingly, this improvement as measured by correlation
639 with ground truth was more pronounced for GABAergic compared to glutamatergic spinal cord
640 neurons (Fig. 4d,e), probably reflecting the higher similarity between glutamatergic spinal cord
641 neurons with (glutamatergic) pyramidal cells from cortex. In addition, we found that high-frequency
642 spiking events were temporally broadened by OASIS but also by default CASCADE (Fig. 5),
643 presumably because both approaches had been optimized for cortical datasets (Fig. 2) and for
644 different calcium kernel decay times (Fig. 3a). For retrained CASCADE, on the other hand, the
645 temporal confinement of spikes during high-frequency spike events as well as their absolute number
646 was more accurately recovered. This absolute number of spikes during such events was still
647 underestimated, as found similarly before (Rupprecht et al., 2021), most likely due to saturation of
648 the calcium indicator. Furthermore, retraining of CASCADE resulted in a less biased estimate of
649 absolute spike rates for both GABAergic and glutamatergic neurons (Fig. 6a-c). Nonetheless, all
650 spike rate inference models proved useful in detecting relative changes in spinal cord neuron spiking,
651 but retrained CASCADE performed slightly better. This performance improvement most likely reflects
652 the previously described suppression of noise by spike rate inference (Pachitariu et al., 2018;
653 Rupprecht et al., 2021). Together, these results highlight the additional benefits in terms of temporal
654 precision and absolute calibration by retraining a supervised algorithm on specific ground truth data.
655 We provide pretrained spike rate inference models for glutamatergic and GABAergic spinal cord

656 neurons together with the underlying ground truth in an easy-to-use repository
657 (<https://github.com/HelmchenLabSoftware/Cascade>).

658 An important observation of our analysis is that spike rates can be readily compared for different
659 temporal segments of the same neuron but not equally well across neurons (Fig. 6d-h). This is not
660 an artifact introduced by spike rate inference, since the effect was similarly present in $\Delta F/F$ data. A
661 potential explanation of this problem is the large variability of spike-triggered $\Delta F/F$ transients across
662 neurons within the same dataset, both for spinal cord and cortex (Fig. 3b,c). This suggests that
663 comparisons of spike rates across neurons may be unreliable, especially for spinal cord dorsal horn
664 due to its high diversity of cell types, but also for data from cortical pyramidal neurons. The origin of
665 this variability is unclear, but it may be due to variable levels of indicator concentrations across cells
666 (Éltes et al., 2019). An alternative and not mutually exclusive explanation is that the determination
667 of the baseline level F_0 to compute $\Delta F/F_0$ is error-prone due to the low baseline fluorescence of
668 GCaMP, thereby inducing biases dependent on bleed-through from surrounding neuropil.
669 Independent of its origin, this variability constitutes a limitation for the inference of absolute spike
670 rates and for the comparison of spiking activity across neurons. This problem has been addressed
671 before by autocalibration in order to identify the unitary response amplitude without ground truth
672 (Deneux et al., 2016; Éltes et al., 2019). While these approaches have so far not been commonly
673 used due to the ambiguity of autocalibration, our study emphasizes the need for improving on such
674 tools to enable quantitative inference of absolute spike rates. We hope that our results and the openly
675 shared CASCADE inference models will encourage future work to calibrate calcium data in other
676 brain regions and to address the remaining limitations due to the variability of spike-triggered calcium
677 responses across neurons.

678 **Contributions**

679 P.R. and A.S. conceived the study. W.F., S.S. and A.S. performed all experiments and pre-analyses.
680 P.R. and A.S. performed quality control. P.R. wrote code, performed analyses and visualized results.
681 P.R., S.S., F.H. and A.S. wrote the paper. F.H. and A.S. supervised the project.

References

- 683
684 Ali, F., Kwan, A.C., 2020. Interpreting in vivo calcium signals from neuronal cell bodies, axons, and dendrites: a review.
685 *Neurophotonics* 7. <https://doi.org/10.1117/1.NPh.7.1.011402>
- 686 Aponte, Y., Bischofberger, J., Jonas, P., 2008. Efficient Ca²⁺ buffering in fast-spiking basket cells of rat hippocampus. *J*
687 *Physiol* 586, 2061–2075. <https://doi.org/10.1113/jphysiol.2007.147298>
- 688 Berens, P., Freeman, J., Deneux, T., Chenkov, N., McColgan, T., Speiser, A., Macke, J.H., Turaga, S.C., Mineault, P.,
689 Rupprecht, P., Gerhard, S., Friedrich, R.W., Friedrich, J., Paninski, L., Pachitariu, M., Harris, K.D., Bolte, B.,
690 Machado, T.A., Ringach, D., Stone, J., Rogerson, L.E., Sofroniew, N.J., Reimer, J., Froudarakis, E., Euler, T.,
691 Román Rosón, M., Theis, L., Tolia, A.S., Bethge, M., 2018. Community-based benchmarking improves spike
692 rate inference from two-photon calcium imaging data. *PLoS Comput Biol* 14.
693 <https://doi.org/10.1371/journal.pcbi.1006157>
- 694 Chen, T.-W., Wardill, T.J., Sun, Y., Pulver, S.R., Renninger, S.L., Baohan, A., Schreiter, E.R., Kerr, R.A., Orger, M.B.,
695 Jayaraman, V., Looger, L.L., Svoboda, K., Kim, D.S., 2013. Ultrasensitive fluorescent proteins for imaging
696 neuronal activity. *Nature* 499, 295–300. <https://doi.org/10.1038/nature12354>
- 697 Christensen, A.J., Iyer, S.M., François, A., Vyas, S., Ramakrishnan, C., Vesuna, S., Deisseroth, K., Scherrer, G., Delp,
698 S.L., 2016. In vivo interrogation of spinal mechanosensory circuits. *Cell Rep* 17, 1699–1710.
699 <https://doi.org/10.1016/j.celrep.2016.10.010>
- 700 Davalos, D., Lee, J.K., Smith, W.B., Brinkman, B., Ellisman, M.H., Zheng, B., Akassoglou, K., 2008. Stable in vivo
701 imaging of densely populated glia, axons and blood vessels in the mouse spinal cord using two-photon
702 microscopy. *J Neurosci Methods* 169, 1–7. <https://doi.org/10.1016/j.jneumeth.2007.11.011>
- 703 Deneux, T., Kaszas, A., Szalay, G., Katona, G., Lakner, T., Grinvald, A., Rózsa, B., Vanzetta, I., 2016. Accurate spike
704 estimation from noisy calcium signals for ultrafast three-dimensional imaging of large neuronal populations in
705 vivo. *Nat Commun* 7, 1–17. <https://doi.org/10.1038/ncomms12190>
- 706 Dibaj, P., Nadrigny, F., Steffens, H., Scheller, A., Hirrlinger, J., Schomburg, E.D., Neusch, C., Kirchhoff, F., 2010. NO
707 mediates microglial response to acute spinal cord injury under ATP control in vivo. *Glia* 58, 1133–1144.
708 <https://doi.org/10.1002/glia.20993>
- 709 Drdla, R., Gassner, M., Gingl, E., Sandkühler, J., 2009. Induction of synaptic long-term potentiation after opioid
710 withdrawal. *Science* 325, 207–210. <https://doi.org/10.1126/science.1171759>
- 711 Éltes, T., Szoboszlai, M., Kerti-Szigeti, K., Nusser, Z., 2019. Improved spike inference accuracy by estimating the peak
712 amplitude of unitary [Ca²⁺] transients in weakly GCaMP6f-expressing hippocampal pyramidal cells. *J Physiol*
713 597, 2925–2947. <https://doi.org/10.1113/JP277681>
- 714 Fan, W., Sdrulla, A.D., 2020. Differential modulation of excitatory and inhibitory populations of superficial dorsal horn
715 neurons in lumbar spinal cord by A β -fiber electrical stimulation. *Pain* 161, 1650–1660.
716 <https://doi.org/10.1097/j.pain.0000000000001836>
- 717 Fan, W., Sullivan, S.J., Sdrulla, A.D., 2022. Dorsal column and root stimulation at A β -fiber intensity activate superficial
718 dorsal horn glutamatergic and GABAergic populations. *Mol Pain* 18, 17448069221079559.
719 <https://doi.org/10.1177/17448069221079559>
- 720 Farrar, M.J., Bernstein, I.M., Schlafer, D.H., Cleland, T.A., Fetcho, J.R., Schaffer, C.B., 2012. Chronic in vivo imaging in
721 the mouse spinal cord using an implanted chamber. *Nat Methods* 9, 297–302.
722 <https://doi.org/10.1038/nmeth.1856>
- 723 Friedenberger, Z., Harkin, E., Tóth, K., Naud, R., 2023. Silences, spikes and bursts: Three-part know of the neural code.
724 *J Physiol* 601, 5165–5193. <https://doi.org/10.1113/JP281510>
- 725 Geppetti, P., Veldhuis, N.A., Lieu, T., Bunnett, N.W., 2015. G protein-coupled receptors: dynamic machines for signaling
726 pain and itch. *Neuron* 88, 635–649. <https://doi.org/10.1016/j.neuron.2015.11.001>
- 727 Giovannucci, A., Friedrich, J., Gunn, P., Kalfon, J., Brown, B.L., Koay, S.A., Taxidis, J., Najafi, F., Gauthier, J.L., Zhou,
728 P., Khakh, B.S., Tank, D.W., Chklovskii, D.B., Pnevmatikakis, E.A., 2019. CalmAn an open source tool for
729 scalable calcium imaging data analysis. *eLife* 8, e38173. <https://doi.org/10.7554/eLife.38173>
- 730 Grienberger, C., Konnerth, A., 2012. Imaging calcium in neurons. *Neuron* 73, 862–885.
731 <https://doi.org/10.1016/j.neuron.2012.02.011>
- 732 Harding, E.K., Boivin, B., Salter, M.W., 2020a. Intracellular calcium responses encode action potential firing in spinal
733 cord lamina I neurons. *J Neurosci* 40, 4439–4456. <https://doi.org/10.1523/JNEUROSCI.0206-20.2020>
- 734 Harding, E.K., Fung, S.W., Bonin, R.P., 2020b. Insights into spinal dorsal horn circuit function and dysfunction using
735 optical approaches. *Front Neural Circuits* 14.
- 736 Häring, M., Zeisel, A., Hochgerner, H., Rinwa, P., Jakobsson, J.E.T., Lönnerberg, P., La Manno, G., Sharma, N.,
737 Borgius, L., Kiehn, O., Lagerström, M.C., Linnarsson, S., Ernfors, P., 2018. Neuronal atlas of the dorsal horn
738 defines its architecture and links sensory input to transcriptional cell types. *Nat Neurosci* 21, 869–880.
739 <https://doi.org/10.1038/s41593-018-0141-1>
- 740 Hoang, H., Sato, M., Shinomoto, S., Tsutsumi, S., Hashizume, M., Ishikawa, T., Kano, M., Ikegaya, Y., Kitamura, K.,
741 Kawato, M., Toyama, K., 2020. Improved hyperacuity estimation of spike timing from calcium imaging. *Sci Rep*
742 10, 17844. <https://doi.org/10.1038/s41598-020-74672-y>

743 Huang, L., Ledochowitsch, P., Knoblich, U., Lecoq, J., Murphy, G.J., Reid, R.C., de Vries, S.E., Koch, C., Zeng, H.,
744 Buice, M.A., Waters, J., Li, L., 2021. Relationship between simultaneously recorded spiking activity and
745 fluorescence signal in GCaMP6 transgenic mice. *eLife* 10, e51675. <https://doi.org/10.7554/eLife.51675>

746 Inoue, M., Takeuchi, A., Manita, S., Horigane, S., Sakamoto, M., Kawakami, R., Yamaguchi, K., Otomo, K., Yokoyama,
747 H., Kim, R., Yokoyama, T., Takemoto-Kimura, S., Abe, M., Okamura, M., Kondo, Y., Quirin, S., Ramakrishnan,
748 C., Imamura, T., Sakimura, K., Nemoto, T., Kano, M., Fujii, H., Deisseroth, K., Kitamura, K., Bito, H., 2019.
749 Rational Engineering of XCaMPs, a Multicolor GECI suite for in vivo imaging of complex brain circuit dynamics.
750 *Cell* 177, 1346-1360.e24. <https://doi.org/10.1016/j.cell.2019.04.007>

751 Ji, N., Freeman, J., Smith, S.L., 2016. Technologies for imaging neural activity in large volumes. *Nat Neurosci* 19, 1154–
752 1164. <https://doi.org/10.1038/nn.4358>

753 Johannssen, H.C., Helmchen, F., 2013. Two-photon imaging of spinal cord cellular networks. *Exp Neurol* 242, 18–26.
754 <https://doi.org/10.1016/j.expneurol.2012.07.014>

755 Johannssen, H.C., Helmchen, F., 2010. In vivo Ca²⁺ imaging of dorsal horn neuronal populations in mouse spinal cord.
756 *J Physiol* 588, 3397–3402. <https://doi.org/10.1113/jphysiol.2010.191833>

757 Kerr, J.N.D., Greenberg, D., Helmchen, F., 2005. Imaging input and output of neocortical networks in vivo. *PNAS* 102,
758 14063–14068. <https://doi.org/10.1073/pnas.0506029102>

759 Kerschensteiner, M., Schwab, M.E., Lichtman, J.W., Misgeld, T., 2005. In vivo imaging of axonal degeneration and
760 regeneration in the injured spinal cord. *Nat Med* 11, 572–577. <https://doi.org/10.1038/nm1229>

761 Koch, S.C., Acton, D., Goulding, M., 2018. Spinal circuits for touch, pain and itch. *Annu Rev Physiol* 80, 189–217.
762 <https://doi.org/10.1146/annurev-physiol-022516-034303>

763 Kumazawa, T., Perl, E.R., 1978. Excitation of marginal and substantia gelatinosa neurons in the primate spinal cord:
764 indications of their place in dorsal horn functional organization. *J Comp Neurol* 177, 417–434.
765 <https://doi.org/10.1002/cne.901770305>

766 Kwan, A.C., Dan, Y., 2012. Dissection of cortical microcircuits by single-neuron stimulation in vivo. *Curr Biol* 22, 1459–
767 1467. <https://doi.org/10.1016/j.cub.2012.06.007>

768 Laffray, S., Pagès, S., Dufour, H., Koninck, P.D., Koninck, Y.D., Côté, D., 2011. Adaptive movement compensation for in
769 vivo imaging of fast cellular dynamics within a moving tissue. *PLoS ONE* 6, e19928.
770 <https://doi.org/10.1371/journal.pone.0019928>

771 Larsson, M., 2017. Pax2 is persistently expressed by GABAergic neurons throughout the adult rat dorsal horn. *Neurosci*
772 *Lett* 638, 96–101. <https://doi.org/10.1016/j.neulet.2016.12.015>

773 Ledochowitsch, P., Huang, L., Knoblich, U., Oliver, M., Lecoq, J., Reid, C., Li, L., Zeng, H., Koch, C., Waters, J., Vries,
774 S.E.J. de, Buice, M.A., 2020. On the correspondence of electrical and optical physiology in in vivo population-
775 scale two-photon calcium imaging. Preprint at <https://www.biorxiv.org/content/10.1101/800102v1> (2019).

776 Lucas-Romero, J., Rivera-Arconada, I., Lopez-Garcia, J.A., 2022. Synchronous firing of dorsal horn neurons at the origin
777 of dorsal root reflexes in naive and paw-inflamed mice. *Front Cell Neurosci* 16.

778 Lucas-Romero, J., Rivera-Arconada, I., Roza, C., Lopez-Garcia, J.A., 2018. Origin and classification of spontaneous
779 discharges in mouse superficial dorsal horn neurons. *Sci Rep* 8, 9735. [https://doi.org/10.1038/s41598-018-
780 27993-y](https://doi.org/10.1038/s41598-018-

780 27993-y)

781 Lütcke, H., Gerhard, F., Zenke, F., Gerstner, W., Helmchen, F., 2013. Inference of neuronal network spike dynamics and
782 topology from calcium imaging data. *Front Neural Circuits* 7. <https://doi.org/10.3389/fncir.2013.00201>

783 Lütcke, H., Murayama, M., Hahn, T., Margolis, D.J., Astori, S., Meyer, S., Göbel, W., Yang, Y., Tang, W., Kügler, S.,
784 Sprengel, R., Nagai, T., Miyawaki, A., Larkum, M.E., Helmchen, F., Hasan, M.T., 2010. Optical recording of
785 neuronal activity with a genetically-encoded calcium indicator in anesthetized and freely moving mice. *Front*
786 *Neural Circuits* 4. <https://doi.org/10.3389/fncir.2010.00009>

787 Maravall, M., Mainen, Z.F., Sabatini, B.L., Svoboda, K., 2000. Estimating intracellular calcium concentrations and
788 buffering without wavelength ratioing. *Biophys J* 78, 2655–2667. [https://doi.org/10.1016/S0006-3495\(00\)76809-
789 3](https://doi.org/10.1016/S0006-3495(00)76809-

789 3)

790 Medrano, M.C., Dhanasobhon, D., Yalcin, I., Schlichter, R., Cordero-Erausquin, M., 2016. Loss of inhibitory tone on
791 spinal cord dorsal horn spontaneously and nonspontaneously active neurons in a mouse model of neuropathic
792 pain. *Pain* 157, 1432–1442. <https://doi.org/10.1097/j.pain.0000000000000538>

793 Milicevic, K.D., Ivanova, V.O., Lovic, D.D., Platisa, J., Andjus, P.R., Antic, S.D., 2024. Plateau depolarizations in
794 spontaneously active neurons detected by calcium or voltage imaging. *Sci Rep* 14, 22787.
795 <https://doi.org/10.1038/s41598-024-70319-4>

796 Misgeld, T., Nikic, I., Kerschensteiner, M., 2007. In vivo imaging of single axons in the mouse spinal cord. *Nat Protoc* 2,
797 263–268. <https://doi.org/10.1038/nprot.2007.24>

798 Moehring, F., Halder, P., Seal, R.P., Stucky, C.L., 2018. Uncovering the cells and circuits of touch in normal and
799 pathological settings. *Neuron* 100, 349–360. <https://doi.org/10.1016/j.neuron.2018.10.019>

800 Nelson, N.A., Wang, X., Cook, D., Carey, E.M., Nimmerjahn, A., 2019. Imaging spinal cord activity in behaving animals. *Exp Neurol*
801 320, 112974. <https://doi.org/10.1016/j.expneurol.2019.112974>

802 Nishida, K., Matsumura, S., Taniguchi, W., Uta, D., Furue, H., Ito, S., 2014. Three-dimensional distribution of sensory
803 stimulation-evoked neuronal activity of spinal dorsal horn neurons analyzed by in vivo calcium imaging. *PLoS*
804 *ONE* 9, e103321. <https://doi.org/10.1371/journal.pone.0103321>

805 Oñativia, J., Schultz, S.R., Dragotti, P.L., 2013. A finite rate of innovation algorithm for fast and accurate spike detection
806 from two-photon calcium imaging. *J Neural Eng* 10, 046017. <https://doi.org/10.1088/1741-2560/10/4/046017>

807 Pachitariu, M., Stringer, C., Dipoppa, M., Schröder, S., Rossi, L.F., Dalgleish, H., Carandini, M., Harris, K.D., 2019.
808 Suite2p: beyond 10,000 neurons with standard two-photon microscopy. Preprint at
809 www.biorxiv.org/content/10.1101/061507v2 (2017).

810 Pachitariu, M., Stringer, C., Harris, K.D., 2018. Robustness of spike deconvolution for neuronal calcium imaging. *J*
811 *Neurosci* 38, 7976–7985. <https://doi.org/10.1523/JNEUROSCI.3339-17.2018>

812 Peirs, C., Dallel, R., Todd, A.J., 2020. Recent advances in our understanding of the organization of dorsal horn neuron
813 populations and their contribution to cutaneous mechanical allodynia. *J Neural Transm* 127, 505–525.
814 <https://doi.org/10.1007/s00702-020-02159-1>

815 Pernía-Andrade, A.J., Goswami, S.P., Stickler, Y., Fröbe, U., Schlögl, A., Jonas, P., 2012. A deconvolution-based
816 method with high sensitivity and temporal resolution for detection of spontaneous synaptic currents in vitro
817 and in vivo. *Biophys J* 103, 1429–1439. <https://doi.org/10.1016/j.bpj.2012.08.039>

818 Pnevmatikakis, E.A., Giovannucci, A., 2017. NoRMCorre: An online algorithm for piecewise rigid motion correction of
819 calcium imaging data. *J Neurosci Methods* 291, 83–94. <https://doi.org/10.1016/j.jneumeth.2017.07.031>

820 Pnevmatikakis, E.A., Soudry, D., Gao, Y., Machado, T.A., Merel, J., Pfau, D., Reardon, T., Mu, Y., Lacefield, C., Yang,
821 W., Ahrens, M., Bruno, R., Jessell, T.M., Peterka, D.S., Yuste, R., Paninski, L., 2016. Simultaneous denoising,
822 deconvolution, and demixing of calcium imaging data. *Neuron* 89, 285–299.
823 <https://doi.org/10.1016/j.neuron.2015.11.037>

824 Ran, C., Hoon, M.A., Chen, X., 2016. The coding of cutaneous temperature in the spinal cord. *Nat Neurosci* 19, 1201–
825 1209. <https://doi.org/10.1038/nn.4350>

826 Rose, T., Goltstein, P.M., Portugues, R., Griesbeck, O., 2014. Putting a finishing touch on GECIs. *Front Mol Neurosci* 7.
827 <https://doi.org/10.3389/fnmol.2014.00088>

828 Rupprecht, P., Carta, S., Hoffmann, A., Echizen, M., Blot, A., Kwan, A.C., Dan, Y., Hofer, S.B., Kitamura, K., Helmchen,
829 F., Friedrich, R.W., 2021. A database and deep learning toolbox for noise-optimized, generalized spike
830 inference from calcium imaging. *Nat Neurosci* 24, 1324–1337. <https://doi.org/10.1038/s41593-021-00895-5>

831 Rupprecht, P., Friedrich, R.W., 2018. Precise synaptic balance in the zebrafish homolog of olfactory cortex. *Neuron* 100,
832 669–683.e5. <https://doi.org/10.1016/j.neuron.2018.09.013>

833 Sandkühler, J., Eblen-Zajjur, A.A., 1994. Identification and characterization of rhythmic nociceptive and non-nociceptive
834 spinal dorsal horn neurons in the rat. *Neuroscience* 61, 991–1006. [https://doi.org/10.1016/0306-4522\(94\)90419-7](https://doi.org/10.1016/0306-4522(94)90419-7)
835 7

836 Sathyamurthy, A., Johnson, K.R., Matson, K.J.E., Dobrott, C.I., Li, L., Ryba, A.R., Bergman, T.B., Kelly, M.C., Kelley,
837 M.W., Levine, A.J., 2018. Massively parallel single nucleus transcriptional profiling defines spinal cord neurons
838 and their activity during behavior. *Cell Rep* 22, 2216–2225. <https://doi.org/10.1016/j.celrep.2018.02.003>

839 Sekiguchi, K.J., Shekhtmeyster, P., Merten, K., Arena, A., Cook, D., Hoffman, E., Ngo, A., Nimmerjahn, A., 2016.
840 Imaging large-scale cellular activity in spinal cord of freely behaving mice. *Nat Commun* 7, 11450.
841 <https://doi.org/10.1038/ncomms11450>

842 Simonetti, M., Hagenston, A.M., Vardeh, D., Freitag, H.E., Mauceri, D., Lu, J., Satagopam, V.P., Schneider, R., Costigan,
843 M., Bading, H., Kuner, R., 2013. Nuclear calcium signaling in spinal neurons drives a genomic program required
844 for persistent inflammatory pain. *Neuron* 77, 43–57. <https://doi.org/10.1016/j.neuron.2012.10.037>

845 Softky, W.R., Koch, C., 1993. The highly irregular firing of cortical cells is inconsistent with temporal integration of
846 random EPSPs. *J Neurosci* 13, 334–350. <https://doi.org/10.1523/JNEUROSCI.13-01-00334.1993>

847 Sullivan, S.J., Sdrulla, A.D., 2022. Excitatory and inhibitory neurons of the spinal cord superficial dorsal horn diverge in
848 their somatosensory responses and plasticity in vivo. *J Neurosci*. 42, 1958–1973.
849 <https://doi.org/10.1523/JNEUROSCI.1860-21.2021>

850 Theis, L., Berens, P., Froudarakis, E., Reimer, J., Román Rosón, M., Baden, T., Euler, T., Tolias, A.S., Bethge, M., 2016.
851 Benchmarking spike rate inference in population calcium imaging. *Neuron* 90, 471–482.
852 <https://doi.org/10.1016/j.neuron.2016.04.014>

853 Tian, L., Hires, S.A., Mao, T., Huber, D., Chiappe, M.E., Chalasani, S.H., Petreanu, L., Akerboom, J., McKinney, S.A.,
854 Schreier, E.R., Bargmann, C.I., Jayaraman, V., Svoboda, K., Looger, L.L., 2009. Imaging neural activity in
855 worms, flies and mice with improved GCaMP calcium indicators. *Nat Methods* 6, 875–881.
856 <https://doi.org/10.1038/nmeth.1398>

857 Todd, A.J., 2017. Identifying functional populations among the interneurons in laminae I–III of the spinal dorsal horn. *Mol*
858 *Pain* 13, 1744806917693003. <https://doi.org/10.1177/1744806917693003>

859 Todd, A.J., Spike, R.C., 1993. The localization of classical transmitters and neuropeptides within neurons in laminae I–III
860 of the mammalian spinal dorsal horn. *Prog Neurobiol* 41, 609–645. [https://doi.org/10.1016/0301-0082\(93\)90045-T](https://doi.org/10.1016/0301-0082(93)90045-T)
861 0082(93)90045-T

862 Warwick, C., Salsovic, J., Hachisuka, J., Smith, K.M., Sheahan, T.D., Chen, H., Ibinson, J., Koerber, H.R., Ross, S.E.,
863 2022. Cell type-specific calcium imaging of central sensitization in mouse dorsal horn. *Nat Commun* 13, 5199.
864 <https://doi.org/10.1038/s41467-022-32608-2>

865 Wei, Z., Lin, B.-J., Chen, T.-W., Daie, K., Svoboda, K., Druckmann, S., 2020. A comparison of neuronal population
866 dynamics measured with calcium imaging and electrophysiology. *PLoS Comput Biol* 16, e1008198.
867 <https://doi.org/10.1371/journal.pcbi.1008198>

868 Xu, Q., Dong, X., 2019. Calcium imaging approaches in investigation of pain mechanism in the spinal cord. *Exp Neurol*
869 317, 129–132. <https://doi.org/10.1016/j.expneurol.2019.03.002>
870 Yaksi, E., Friedrich, R.W., 2006. Reconstruction of firing rate changes across neuronal populations by temporally
871 deconvolved Ca²⁺ imaging. *Nat Methods* 3, 377–383. <https://doi.org/10.1038/nmeth874>
872 Zhang, Y., Rózsa, M., Liang, Y., Bushey, D., Wei, Z., Zheng, J., Reep, D., Broussard, G.J., Tsang, A., Tsegaye, G.,
873 Narayan, S., Obara, C.J., Lim, J.-X., Patel, R., Zhang, R., Ahrens, M.B., Turner, G.C., Wang, S.S.-H., Korff,
874 W.L., Schreier, E.R., Svoboda, K., Hasseman, J.P., Kolb, I., Looger, L.L., 2023. Fast and sensitive GCaMP
875 calcium indicators for imaging neural populations. *Nature* 615, 884–891. [https://doi.org/10.1038/s41586-023-](https://doi.org/10.1038/s41586-023-05828-9)
876 05828-9
877 Zhou, Z., Yip, H.M., Tsimring, K., Sur, M., Ip, J.P.K., Tin, C., 2023. Effective and efficient neural networks for spike
878 inference from in vivo calcium imaging. *Cell Rep Methods* 3, 100462.
879 <https://doi.org/10.1016/j.crmeth.2023.100462>
880

881

JNeurosci Accepted Manuscript

Figure and table legends

883

884

885

886

887

888

889

890

891

892

893

894

Figure 1 | Simultaneous recording of electrophysiological spikes and calcium signals in glutamatergic and GABAergic neurons of mouse spinal cord. **a**, Scheme of transgenic expression of GCaMP6s in glutamatergic (blue) or GABAergic neurons (red) in mouse spinal cord. **b**, Lumbar spinal cord explant preparation used for ground truth recordings with simultaneous two-photon calcium imaging and cell-attached recordings. **c**, Example FOV for a slow recording (2.5 Hz) for glutamatergic neurons (*VGlu2*). The sub-area highlighted by the dashed rectangle indicates the FOV for a faster recording (>30 Hz) from the same neuron. **d**, Same as in (c) but for a GABAergic neuron (*Viaat*). **e-g**, Examples of ground truth recordings from three glutamatergic neurons, with zoom-in to a subregion below. For each recording, the normalized fluorescence extracted from calcium imaging ($\Delta F/F$), the smoothed spike rate derived from electrophysiological spike times (*SR*), and the spike times detected from the electrophysiological recording (*Spikes*) are shown. **h-j**, Same as in (e-g) but for three example GABAergic neurons. Red flashes indicate times when dorsal root stimulation was applied. For similar example recordings from mouse cortex, see Fig. 1-1.

895

896

897

898

899

900

901

902

Table 1 | Overview of recorded ground truth datasets. The first data row indicates the recording characteristics for GABAergic neurons, the second data row the recording characteristics for glutamatergic neurons. Recordings with large FOVs and low frame rates (<3 Hz) exhibit higher noise levels compared to zoomed-in FOVs with higher frame rates (>30 Hz), as described in the main text. The total recording duration (third column) is the recording duration for both slow (<3 Hz) and fast (>30 Hz) recordings. The last column (“Spikes within bursts”) quantifies the fraction of spikes with neighboring spikes closer than 10 ms. Values are displayed as mean \pm standard deviation, except for spike rate and spikes within bursts, which are reported as medians with interquartile ranges. Standardized noise levels were computed as the median absolute fluctuations of $\Delta F/F$, normalized by the imaging frame rate (Methods).

903

904

905

906

907

908

909

910

911

912

913

914

915

916

917

918

919

920

921

922

Figure 2 | Comparison of electrophysiological characteristics of ground truth recordings from spinal cord and cortex. **a**, Spike rates for spinal cord glutamatergic neurons ground truth (*SC Glu+*, blue), spinal cord GABAergic neurons ground truth (*SC GABA+*, red), both recorded for this study with GCaMP6s, and excitatory neurons in transgenic mouse cortex that express GCaMP6s or GCaMP6f (*Cortex*, black). Statistics based on spinal cord recordings encompassing data from both spontaneous and dorsal root stimulation periods are shown as solid boxplots (full dataset); statistics based on spontaneous data only while excluding stimulation periods are shown with transparent color (spontaneous dataset). Cortex data comprise both spontaneous activity and activity evoked by visual stimulation. Each data point underlying the box plot represents a recorded neuron ($n = 21, 23$ and 80 neurons for *SC Glu+*, *SC GABA+* and *Cortex*). Spike rates of *SC Glu+* were higher than for *SC GABA+* and *Cortex* ($p_{\text{full}} = 0.001$ and 0.000001 based on full spinal cord recordings; Wilcoxon rank sum test; p -values when based on spontaneous periods only, p_{spont} , were unchanged to the reported digit compared to p_{full}), with no significant difference between *SC GABA+* and *Cortex* ($p_{\text{full}} = 0.83$, $p_{\text{spont}} = 0.76$). **b**, Cumulative distribution of the temporal distance from each spike to the neighboring spike, as a measure of burstiness. Spinal cord spike patterns exhibit lower burstiness compared to spike patterns from the cortex dataset. Each thin line indicates the cumulative distribution of these distances from all spikes of an individual neuron. Bold lines indicate the average across neurons within a dataset. **c**, Coefficient of variation (CoV) of inter-spike intervals (ISIs) as an additional measure of burstiness. Higher CoV indicates higher burstiness, lower CoV a less bursty and more regular spike pattern. As in (a), each datapoint is from an individual neuron, and transparent boxplots are computed from spontaneous activity periods only. CoV was significantly higher for the cortex dataset, reflecting higher burstiness ($p_{\text{full}} < 10^{-6}$, $p_{\text{spont}} < 10^{-6}$; Wilcoxon ranksum test); no difference between spinal cord datasets was found ($p_{\text{full}} = 0.24$; $p_{\text{spont}} = 0.13$). * $p < 0.05$, ** $p < 0.01$, *** $p < 0.001$, n.s., not significant ($p > 0.05$).

923

924

925

926

927

928

929

930

931

932

933

Figure 3 | Comparison of the spike-calcium relationship of ground truth recordings from spinal cord and cortex. **a**, Calcium response ($\Delta F/F$) for the average action potential across neurons, computed by linear deconvolution of the ground truth recording, at the common sampling rate of 2.5 Hz. Note that this kernel was derived from all spikes, not only from isolated spikes. Shown is median and quartile corridors across all neurons ($n = 21, 23$ and 80 for the glutamatergic, GABAergic and cortex datasets). For the temperature-dependence of the kernel, see Fig. 3-1. **b**, Mean calcium response ($\Delta F/F$) during the first 2 s after $t = 0$ s for the average action potential across neurons. Please note the logarithmic y-scale. No significant difference between *SC Glu+* and *SC GABA+* ($p = 0.69$) *SC Glu+* and *Cortex* ($p = 0.17$) or *SC GABA+* and *Cortex* ($p = 0.06$, Wilcoxon rank sum test). **c**, Peak calcium response ($\Delta F/F$) for the average action potential across neurons. Please note the logarithmic y-scale. No significant difference between *SC Glu+* and *SC GABA+* ($p = 0.52$), but increase of *Cortex* compared to *SC Glu+* ($p = 0.0071$) or *SC GABA+* ($p = 0.0049$, Wilcoxon rank sum test). **d**, Illustrative simulation of $\Delta F/F$ traces with typical noise levels and calcium transients evoked by average (median) amplitude (*SC Glu+*

934 kernel in panel (a)). The simulated recording conditions are 40 Hz imaging rate and a standardized noise level (Methods)
935 of “1.0” for the upper trace, and 2.54 Hz and noise level of “5.0” for the lower trace. Spike-evoked calcium transients can
936 be clearly observed for a large number of simultaneous spikes but not distinguished from noise for single spikes. **e**, The
937 experimental $\Delta F/F$ values are predicted by the convolution of spike times with the linear kernel (from panel (a)). The plot
938 indicates how well a neuron-specific linear forward model fits the experimental data. Each visualized data point is a
939 timepoint from a ground truth recording downsampled to 3 Hz (number of timepoints: 27’816 for Glu⁺, 28’835 for
940 GABA⁺, 31’613 for cortex). * $p < 0.05$, ** $p < 0.01$, *** $p < 0.001$, n.s., not significant ($p > 0.05$).

941 **Figure 4 | Spike rate inference algorithms in spinal cord neurons.** **a**, Schematic of five different approaches that can
942 be used as a proxy readout for neuronal spike rates: (1) Raw $\Delta F/F$ (green), (2) Spike rate inference with CASCADE, trained
943 on a diverse ground truth dataset that mostly consists of cortical excitatory neurons (black), (3) Spike rate inference with
944 CASCADE, trained on a ground truth dataset with glutamatergic spinal cord neurons (blue), (4) Spike rate inference with
945 CASCADE, trained on a ground truth dataset with GABAergic spinal cord neurons (red), (5) Unsupervised spike rate
946 inference using OASIS, implemented in Suite2p (magenta). **b**, Examples of an extracted ground truth recording together
947 with the ground truth spike rate and spike rate predictions with default and retrained CASCADE, as well as OASIS. Sampled
948 at 30 Hz with a standardized noise level of “7”, from an excitatory neuron. The same ground truth with spike rate predictions
949 resampled at 2.5 Hz are shown in Fig. 4-1. **c**, Zoom-in to sub-regions in (b), highlighting the differences of predictions for
950 high-frequency spike events. **d-f**, Quantification of performance of the five approaches described in (a) for the glutamatergic
951 spinal cord dataset (d) and the GABAergic spinal cord dataset (e) and the cortex dataset (f). Each datapoint underlying the
952 boxplots is a ground truth recording from a different neuron ($n = 21, 23$ and 80 for glutamatergic, GABAergic and cortex
953 datasets). Ground truth was resampled at 30 Hz at a standardized noise level of “7” (see Methods). Performance was
954 evaluated after correction for systematic delays (Fig. 4-2). Outcomes of relevant statistical tests are reported in the main
955 text. **g**, Quantification of performance for the GABAergic spinal cord dataset across sampling rates, normalized for the
956 performance of the default CASCADE model. The same quantification for the glutamatergic spinal cord dataset is shown
957 in Fig. 4-3a. Color code as in (a-d). **h**, Quantification of performance for the GABAergic spinal cord dataset across noise
958 levels. The same quantification for the glutamatergic spinal cord dataset is shown in Fig. 4-3b. The dependence of
959 performance improvements on cellular characteristics is analyzed in Fig. 4-4.

960 **Figure 5 | Spike rate inference for high-frequency spike events for glutamatergic neurons in spinal cord.** **a-e**, High-
961 frequency spike events for the glutamatergic neuron dataset, with the corresponding associated ground truth spike rate
962 (a), $\Delta F/F$ signal (b), spike rate inferred by the default CASCADE model (c), spike rate inferred from the retrained CASCADE
963 model (SC Glu⁺ CASCADE) (d), and spike rate inferred by the OASIS algorithm (e). **f-j**, Same as in (a-e) but averaged
964 across events, with absolute values indicated if possible. Prolonged spike rate is seen for the default CASCADE and OASIS
965 models. The median number of spikes during events (1-s window around event) for ground truth vs. default CASCADE vs.
966 retrained CASCADE is 13.6 vs. 7.9 vs. 9.4 spikes. The same analyses for GABAergic neurons in spinal cord are shown in
967 Fig. 5-1.

968 **Figure 6. Inference of absolute and relative spike rates with CASCADE.** **a**, Illustration of both types of errors, false
969 positives (blue) and false negatives (orange). Ground truth in red, inferred spike rate in black. **b**, False positives and
970 negatives for the default (black) and the retrained (red) SC GABA⁺ CASCADE model. The evaluation time window indicates
971 the binning of inferred spike rates before false positives/negatives were computed as shown in (a). Therefore, the values
972 for the longest evaluation time window indicate the overall bias towards false positives or false negatives. This case is
973 additionally illustrated as a box plot on the right side to provide statistics across neurons ($n = 23$ neurons). **c**, As in (b), but
974 for glutamatergic neurons ($n = 21$ neurons) and with the retrained SC GABA⁺ CASCADE model. **d**, Illustration of division
975 of each recording in 5-s segments for ground truth, $\Delta F/F$ and inferred spike rate traces. The goal is to test whether inferred
976 spike rate (SR) correctly recovers whether the ground truth spike rate (GT) within a random 5-s segment x is larger than
977 the true spike rate in another segment y . **e**, Percentage of correct spike rate comparisons as described in (d) for both
978 datasets and all approaches. Compared segments are taken from different neurons. Statistics across $n = 506$ and $n = 420$
979 neuron pairs for the GABAergic and glutamatergic datasets. Outcomes of relevant statistical tests are reported in the main
980 text. **f**, Percentage of correct spike rate comparisons as described in (d) for both datasets and all approaches. Compared
981 segments are taken from the same neuron. Statistics across $n = 23$ and $n = 21$ neurons for the GABAergic and
982 glutamatergic datasets. **g**, Comparison of average true and inferred spike rates across neurons. **h**, Differences between
983 true spike rates of two neurons (x -axis) vs. differences between inferred spike rates of the same neurons (y -axis, top row)
984 or $\Delta F/F$ values (y -axis, bottom row).

985 **Figure 7. Spike rate inference from population calcium imaging in mouse spinal cord.** **a**, Experimental preparation
986 for cell-type specific in vivo two-photon imaging of mouse spinal cord in transgenic mice during anesthesia. **b**, Example
987 FOV during imaging of glutamatergic spinal cord neurons. **c**, Example FOV during imaging of GABAergic spinal cord
988 neurons. **d**, Extracted $\Delta F/F$ traces (red) and deconvolved spike rates (black) from a subset of the GABAergic neuron ROIs
989 from (c). Deconvolution performed with the SC GABA⁺ CASCADE model. **e**, Extracted $\Delta F/F$ traces (blue) and deconvolved
990 spike rates (black) from a subset of the glutamatergic neuron ROIs from (b). Deconvolution performed with the SC Glu⁺
991 CASCADE model. **f**, Zoom-in to a $\Delta F/F$ trace and estimated spike rate for a GABAergic neuron in (d). The number of
992 spikes (action potentials, “APs”) is indicated below events. Subevents are shaded with different gray values. **g-h**, Same as
993 (f) but for glutamatergic neurons in (e). **i**, Mean spike rates of neurons detected from the FOVs in (b,c) during shallow (1%
994 isoflurane) vs. deep (2%) anesthesia, with decreased spike rates for deep anesthesia for both cell types (*, $p = 0.040$,
995 Wilcoxon ranksum test, 23 neurons for the glutamatergic dataset; ***, $p = 0.000016$, 48 neurons for the GABAergic
996 dataset).

997

JNeurosci Accepted Manuscript

998

	Number of neurons	Total recording duration (min)	Recording duration (<3 Hz) (min)	Noise (<3 Hz) (%·Hz ^{-1/2})	Recording duration (>30 Hz) (min)	Noise (>30 Hz) (%·Hz ^{-1/2})	Spike rate (Hz)	Spikes within bursts (%)
GABAergic neurons	23	9.6 ± 3.7	4.6 ± 1.6	4.3 ± 1.1	4.9 ± 1.9	1.0 ± 0.3	1.1 [0.5–1.7]	6.5 [3.1–11.4]
Glutamatergic neurons	21	10.7 ± 6.0	5.0 ± 3.3	7.2 ± 2.9	5.7 ± 2.9	1.0 ± 0.2	3.7 [2.8–6.3]	16.0 [3.8–35.5]

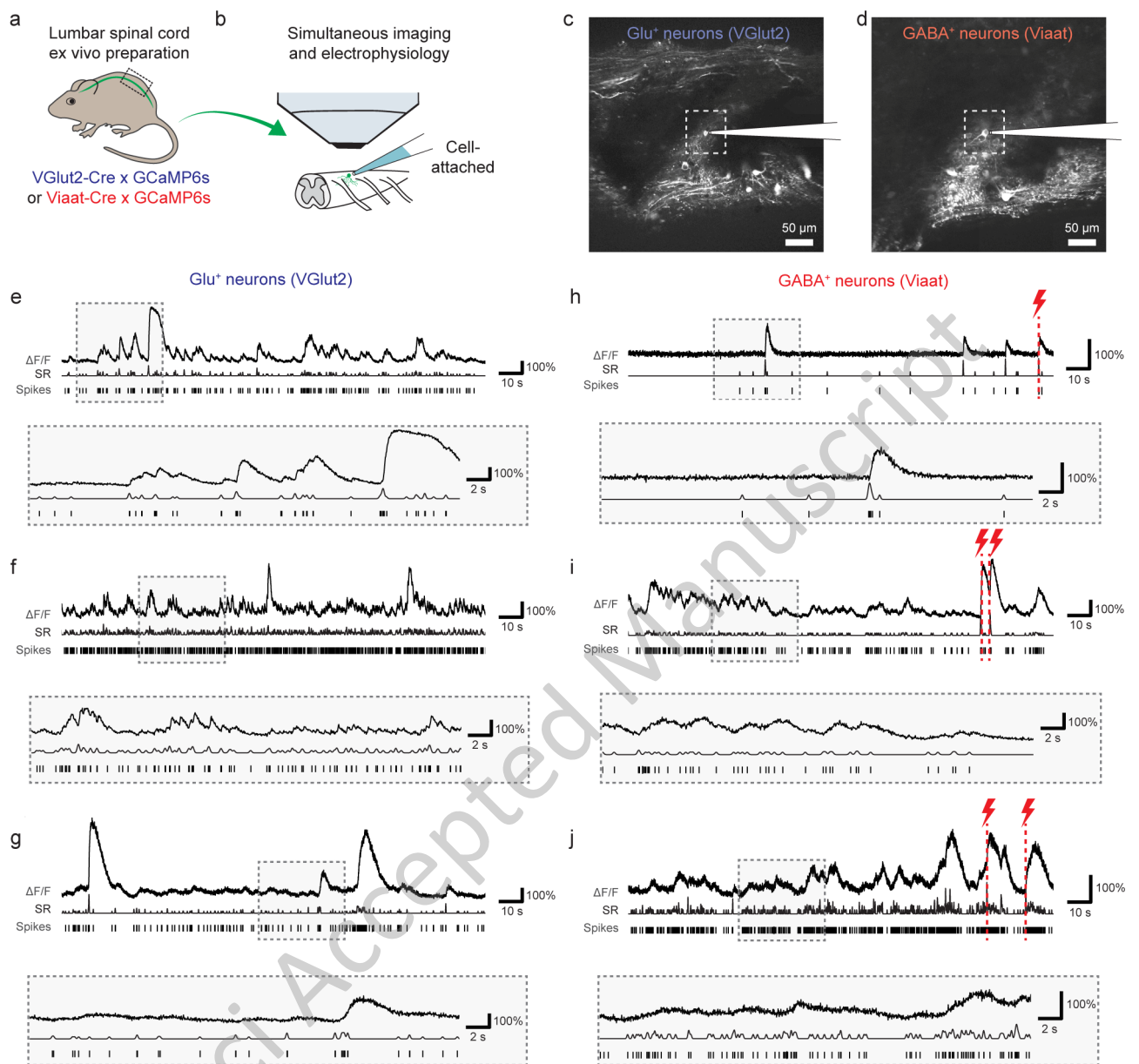
999

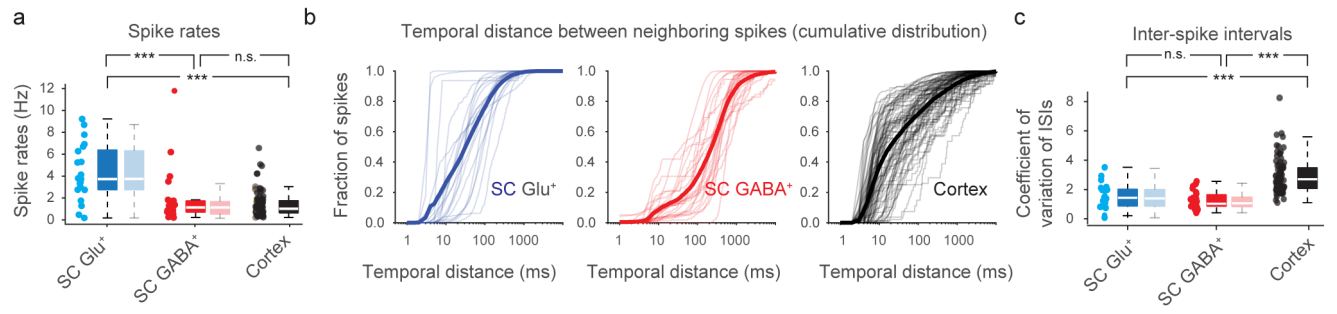
1000

1001

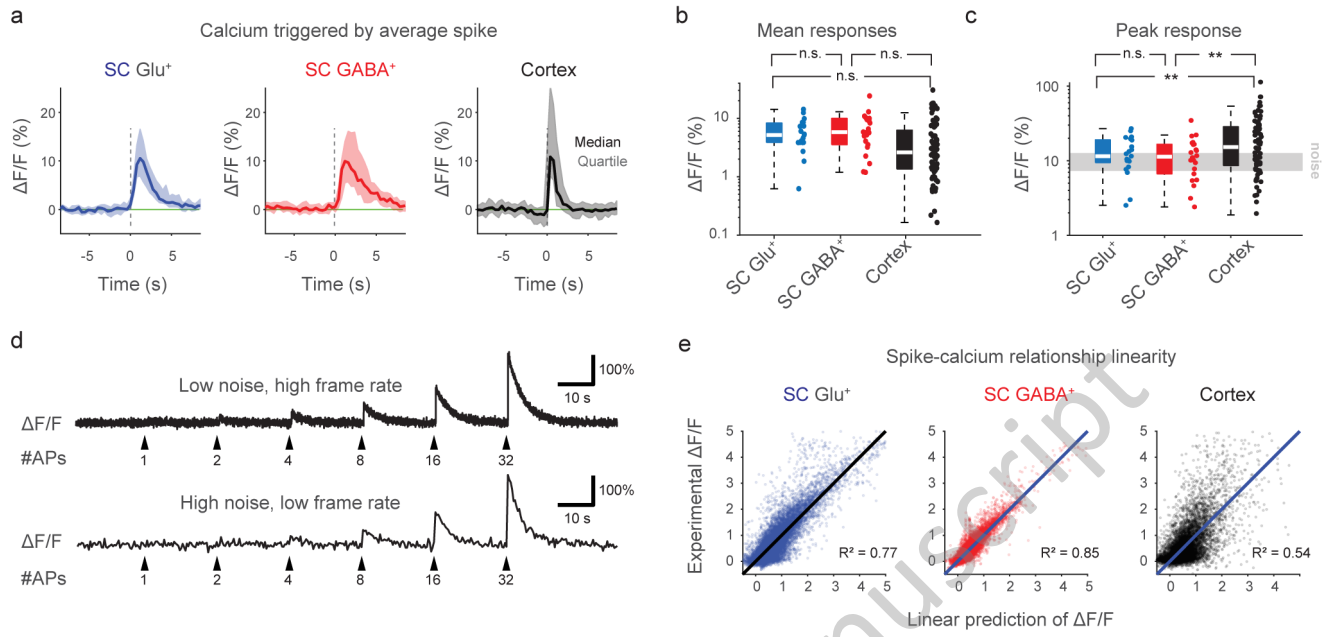
1002

JNeurosci Accepted Manuscript





JNeurosci Accepted Manuscript

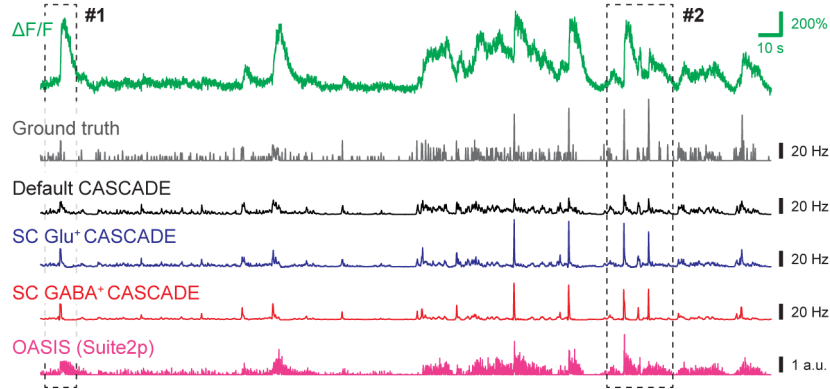


JNeurosci Accepted Manuscript

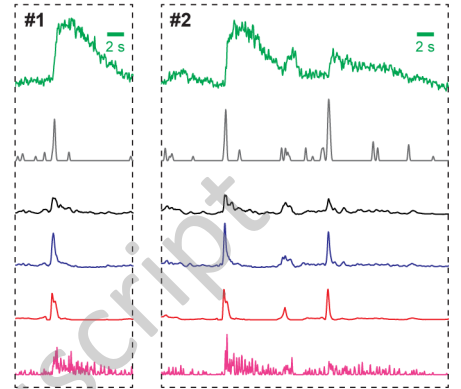
a



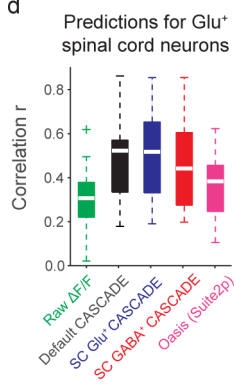
b



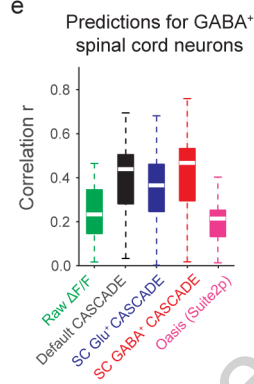
c



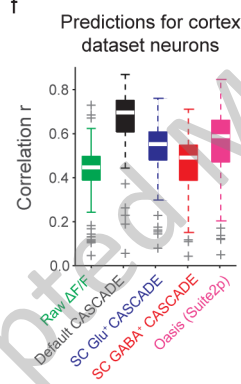
d



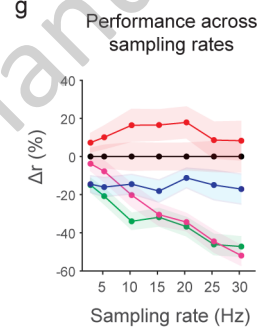
e



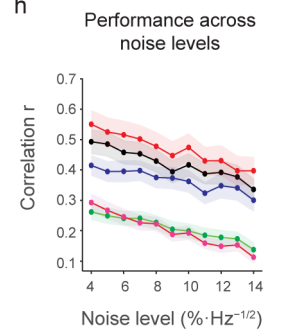
f



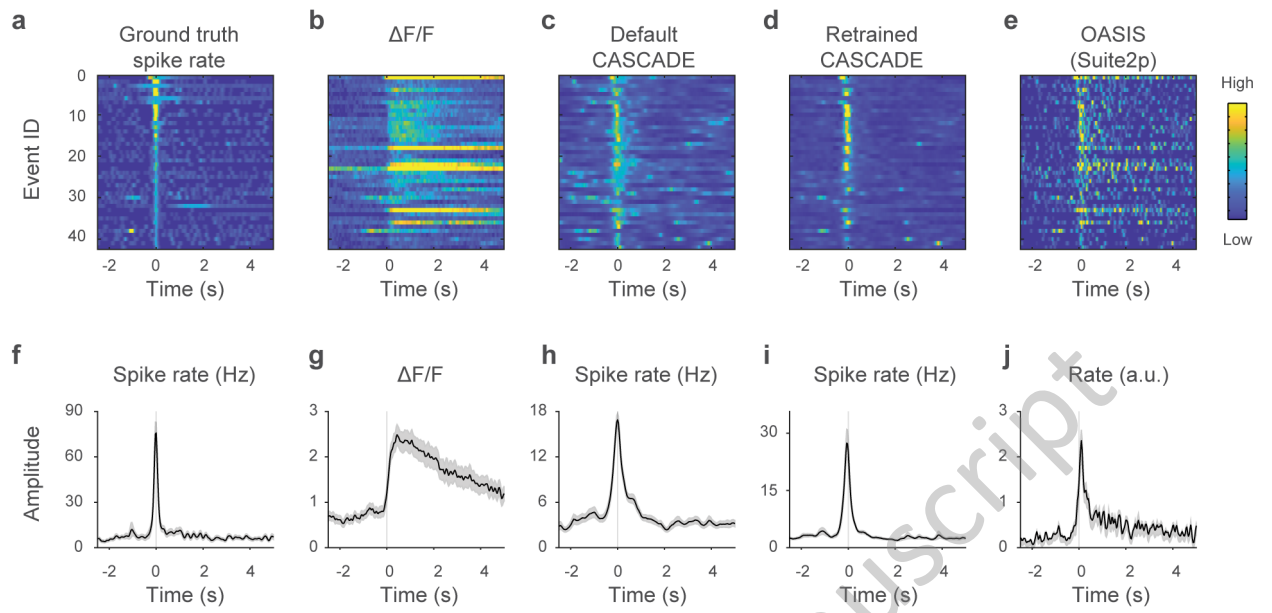
g



h



JNeurosci Accepted Manuscript



JNeurosci Accepted Manuscript

